

**Using fusion-product spectroscopy to diagnose
inertial confinement fusion implosions and study
stopping power on OMEGA, the NIF, and Z**

by

Brandon Lahmann

B.S., Missouri University of Science and Technology (2013)

M.S., Missouri University of Science and Technology (2014)

Submitted to the Department of Nuclear Science and Engineering
in partial fulfillment of the requirements for the degree of

Doctor of Science in Nuclear Science and Engineering

at the

MASSACHUSETTS INSTITUTE OF TECHNOLOGY

February 2021

© Massachusetts Institute of Technology 2021. All rights reserved.

Author
Department of Nuclear Science and Engineering
January 22, 2021

Certified by
Johan Frenje
Senior Research Scientist
Thesis Supervisor

Accepted by
Probably some old white dude
Chairman, Department Committee on Graduate Theses

**Using fusion-product spectroscopy to diagnose inertial
confinement fusion implosions and study stopping power on
OMEGA, the NIF, and Z**

by

Brandon Lahmann

Submitted to the Department of Nuclear Science and Engineering
on January 22, 2021, in partial fulfillment of the
requirements for the degree of
Doctor of Science in Nuclear Science and Engineering

Abstract

Abstract text goes here

Thesis Supervisor: Johan Frenje
Title: Senior Research Scientist

Acknowledgments

This is the acknowledgments section. You should replace this with your own acknowledgments.

Contents

Acknowledgments	5
Thesis Overview	17
1 Introduction	19
1.1 Physics of Nuclear Energy	30
1.2 Inertial Confinement Fusion	35
1.3 Magnetized Liner Inertial Fusion	41
1.4 Experimental Facilities	45
1.4.1 MIT High Energy Density Physics (HEDP) Accelerator Facility	45
1.4.2 The OMEGA Laser Facility	45
1.4.3 The Z Pulsed Power Facility	46
1.4.4 The National Ignition Facility	46
2 Secondary DT Neutron Measurements on the NIF	49
2.1 Secondary Nuclear Reactions	49
2.1.1 Introduction	49
2.1.2 Yield Ratios	50
2.1.3 Secondary Spectra	53
2.2 Simulating Secondary Nuclear Reactions	54
2.2.1 Monte Carlo Model for Tracing Particles Through a Plasma .	55
2.2.2 Profile Effects	63
2.2.3 Asymmetry Effects	64

2.3	Measuring Secondaries on the NIF	64
3	title	65
3.1	Basic Conceptual Design	66
3.2	Proof-of-Principle Design	68
3.3	Shielded Annular Foil Design	70
3.3.1	Internal Shielding	71
3.3.2	External Shielding	72
3.3.3	Final Conceptual Design	75
3.3.4	Design Tolerances and Sensitivities	75
3.4	Conclusions	78
A	Secondary Reaction Energy Derivation	81

List of Figures

1-1	Three Gorges Dam	20
1-2	San Gorgonio Pass Wind Farm	21
1-3	Serpa solar power plant	23
1-4	Missouri University of Science & Technology Nuclear Reactor Core .	25
1-5	The Sun	27
1-6	Mass per nuclide of various isotopes. All exothermic fusion reactions must occur between isotopes lighter than ^{56}Fe and all exothermic fission reactions must occur between isotopes heavier than ^{56}Fe	31
1-7	Fusion Cross-Sections	33
1-8	Fusion Reactivities	35
1-9	Hot Spot Ignition Scheme	37
1-10	ICF Fusion Requirements	39
1-11	Direct Drive Schematic	41
1-12	Indirect Drive Schematic	42
1-13	Z-pinch or MagLIF	42
1-14	Accelerator	45
1-15	OMEGA Laser	46
1-16	Z Machine	46
2-1	Secondary fusion cross sections	51
2-2	Secondary Product Yield Ratios	52
2-3	Secondary DT neutron angle-energy relationship	53
2-4	Secondary DT neutron spectra for varying areal densities	53

- 3-4 SOLIDWORKS drawing of the neutron recoil-spectrometer fielded on the Z facility for shot z3135. The spectrometer consisted of a CH₂ conversion foil (yellow) and CR-39 detector (teal) all contained within an aluminum tube (gray) housing structure. The foil was 10 μm thick and positioned 25 cm away from the CR-39 detector. These parameters were chosen in an attempt to measure the ion temperature. This was done before the CR-39 broadening was well characterized. 68
- 3-5 DDn spectrum from shot z3135, measured by the proof-of-principle neutron recoil-spectrometer shown in Figure 3-4. The spectrum was determined from the CR-39 detector after using CCT to reduce the neutron background. The red data points are the raw data and the black dashed curve is a Gaussian fit to the main peak. The yield under the Gaussian is between 1.7×10^{12} and 2.8×10^{12} depending on the modeling of the scattering environment. The yield as inferred by indium activation was roughly 3.0×10^{12} . The FWHM of the Gaussian fit was 528 keV. 69
- 3-6 SOLIDWORKS drawing of the neutron-recoil-spectrometer proposed for the Z facility. The CR-39 detector (teal) is shielded from direct line-of-sight neutrons by a polyethylene plug (red) directly in front. The conversion foil (yellow) is annular and separated from shielding plug by a thin sheet of aluminum. This prevents recoil-protons created within the shield from reaching the CR-39 detector. The whole system is contained within an aluminum housing (gray) which is itself surrounded by a layer of polyethylene (blue) to shield again external neutron scatter sources. The outer surface of the aluminum housing is conical with respect to TCC so as to reduce the amount of neutron-scatter caused by the spectrometer itself. 70

List of Tables

1.1	Mass differences and energy released by various reactions	30
1.2	Short hand notations for a few light isotopes of particular interest to nuclear fusion	31
3.1	Parameters used in MCNP6 to model the geometry depicted in Figure 3-8. All cylinders are centered about TCC.	73
3.2	$(S/B)_{dsr}$ inferred from MCNP6 once external scattering sources are considered. Simulations were done without any external shielding and otherwise used parameters listed in Table 3.1 and Table 3.3.	73
3.3	Design parameters of the final conceptual design of the neutron-recoil-spectrometer. The slopes of the internal shield and the external surface of the housing is such that it would intersect with TCC if extended. The slopes of the internal surface of the housing and the external shielding match that of the external surface of the housing.	76
3.4	Performance metrics for the next neutron-recoil-spectrometer. Simulations were done using parameters listed in Table 3.1 and Table 3.3.	77
3.5	Design sensitivities for the next neutron-recoil-spectrometer. Sensitivities come from linear fits to several simulations within the specified range.	77

Thesis Overview

1 | Introduction

Ever since the Industrial Revolution, the energy consumption of the World has done nothing but rise over time. [?] This rise in energy consumption correlates well with a rise in quality of life seen throughout the years. [?] We will therefore take it as an axiom that the continued increase in energy consumption is not only inevitable but also desirable for the Net Good of Humanity. It is worth noting that the distribution of energy consumption and the efficiency of energy consumption are both extremely important topics in and of themselves, but unfortunately are beyond the scope of this discussion. This situation means that energy production must also continue to rise so as to meet the growing demand.

Unfortunately, time has quickly shown that our current forms of energy production are not sustainable. [?] The vast majority of energy produced today comes from *fossil fuels*; materials such as coal, oil, and natural gas. [?] These fuels are formed by natural processes that take place over time periods on the order of millions of years. [?] Due to this extremely long production time, our consumption has far outpaced it leading to these fuels being classified as *non-renewable*. [?] This would not be intrinsically bad if the source was effectively infinite, but most research estimates that these resources can only last on the order of 100 years at current consumption rates. [?] This finite supply has already lead to a handful of *energy crises* over the years. [?]

Even more important than the limited theoretical supply is the environmental impacts of these fuels. Massive amounts of carbon dioxide (CO_2) are released into the environment every year due to the burning of fossil fuels. [?] Research has repeatedly shown that this emission is having harmful, non-reversible impacts on the

environment. [?] Several countries have deemed this to be undesirable and have taken a variety of actions to reduce future releases of CO₂. [?] These actions serve to limit the amount of fossil fuels that can be burnt, which even further limits the ability of fossil fuels to meet our growing demand. It is therefore, extremely desirable to develop alternative *renewable* energy sources that can meet our demands without producing exorbitant amounts of CO₂.

Thankfully, there are a handful of different energy sources that meet these requirements, each with their own advantages and disadvantages. They are hydroelectric, wind, solar, nuclear fission, and nuclear fusion.

Hydroelectric Power

Hydroelectric power is generated from dams built along the path of rivers. Gravity forces the water to descend through the dam where it passes through and spins a turbine. The spinning turbine drives an electric generator creating the electricity.



Figure 1-1: The Three Gorges Dam in Sandouping, China is the world's largest power generating station of any kind. It generates 22,500 MW of electricity from the Yangtze River. [? ? ?]

Hydroelectric is considered a renewable resource because the source for a given dam is effectively infinite. [?] Because there is no steam involved, they are highly

efficient, only having to convert kinetic energy to electricity. [?] Dams generate large amounts of power at competitive costs to fossil fuels [?] and are generally always available. [?] Additionally, they can be highly flexible with their power outputs allowing them to follow variable demands. [?] All of this without the consequence of releasing CO₂ into the environment. [?]

The primary disadvantage of hydroelectric power is the number of suitable locations for dams is finite. [?] While for most countries, there is still room for expansion today [?], it will not be sufficient to meet growing power demands indefinitely. So while hydroelectric is an extremely attractive source of clean renewable energy, it alone cannot serve to meet our energy needs.

Wind Power

Wind power is generated by large windmills whose blades turn when struck by wind. The spinning blades ultimately turn a turbine which goes on to produce electricity through an electric motor. [?]



Figure 1-2: San Gorgonio Pass Wind Farm located in Riverside County California. The farm consists of 3,218 units delivering a total of 615 MW. [? ?]

Like hydroelectric, wind is clearly a renewable resource and windmills have no associated CO₂ production with operation. [?] Like hydroelectric, no steam is involved in the energy conversion process so it can be made high efficient. [?]

Wind power does have a handful of disadvantages when compared to fossil fuels. First off, wind is not always available and when it is speeds are variable. This means wind cannot be used as a so called *base load* energy source.[?] Base load sources are those that can produce electricity nearly indefinitely to meet the minimum demand of the grid at all times. [?] Wind's variable often unpredictable nature means the produced energy often needs to be stored in some way, increasing operational costs. [?] Cost comparisons with fossil fuels vary, but generally wind is considered to be more expensive; although not intolerably so. [?]

Another disadvantage of wind power is it's energy density, the amount of energy it can produce per unit area required to operate. On average, a single windmill produces on the order of **2 MW** while occupying an area on the order of **1.5 acres** with a capability factor (fraction of time producing power) of roughly **33%** . [?] For reference the average power consumption of the United States was **482 GW** in 2018 [?] meaning over **1500** square miles (more than a Rhode Island of area) would be required to power the country on wind alone. **Sources vary greatly on this, consider removing.**

One final disadvantage of wind power is the environmental impact it has. Windmills have been shown to be harmful to birds [?] and are generally unattractive to humans aesthetically. [?] Given the large volume they consume, this can quickly become problematic.

All in all, wind is a renewable energy source but has several issues with it's implementation. While it certainly can hold a place in the energy profile of a pure renewable energy grid, it cannot meet the demand reliably alone.

Solar Power

Solar power largely refers to a variety of technologies that convert radiation from the sun into electricity. [?] While the exact method for extracting electricity varies

between different technologies, for the purposes of this discussion they largely have the same advantages and disadvantageous.



Figure 1-3: Serpa solar power plant located in Serpa, Portugal. The plant consists of 52,300 units and supplies a total of 11 MW. [? ?]

Like all the other forms of power generation mentioned thus far, the sun is clearly a renewable source of energy. And like the other renewable sources of energy, no CO₂ emissions are required in the conversion to electricity.

The disadvantages of solar power are very similar to those discussed with wind power. Solar power only works when the sun is out and even then, can be intermittently interrupted by inopportune weather. [?] This makes solar power unattractive as a base load option and necessitates energy storage capabilities.

Like wind energy, solar also has a limited energy density. The sun's intensity on earth is about **1.36 kW per square meter** and the efficiency of solar panels is of the order of **15%**. [?] This means you'd need over **1000 square miles** of constant sunlight to power the United States. Accounting for the capability factor brings this estimate up by a factor of 2 or 3.

Like wind, solar energy certainly has a place but cannot meet the growing energy demand on its own.

Nuclear Fission

Nuclear fission refers to the process of fragmenting large atoms (typically masses of the order 200 amu) into smaller constituents. [?] This releases a significant amount of energy (the physics of which we'll discuss in Section ??) which can then be used to heat water and generate electricity through the well known Carnot cycle. [?] In fact, the way electricity is produced from nuclear fission is exactly identical to typical fossil fuel plants, the only difference being the source of heat.

When compared to fossil fuels, nuclear fission power has a couple of key advantageous. Firstly, fission generates no CO₂ making it a source of clean energy. [?] Secondly, the energy density of nuclear fission is orders of magnitude above that of fossil fuels. The potential energy density of UO₂ (the fuel used in nuclear reactors) is roughly 7.1×10^7 MJ/kg [?]. The energy density for coal and methane is only 15 and 55 MJ/kg respectively. [?] This means the costs of fuel is practically non-existent for nuclear reactors, with most of the costs being capital cost in constructing the reactor. [?] Additionally, the costs of nuclear energy tends to be competitive with fossil fuels when balanced over the life of the reactor. [?]

Nuclear fission power also has a couple of advantages over the traditional renewable energy sources as well. Unlike solar and wind, nuclear power excels as a base load energy production option, often running continuously for 18 months at a time. [?] Nuclear power is also traditionally cheaper than solar and wind [?], although over recent years the two have become much more competitive. [?] Unlike hydroelectric, expanding nuclear power is only limited by the high investment costs needed to build new plants.

There are, however, disadvantages associated with nuclear fission power. One is the public perception of its safety is not remarkable after the accidents at Chernobyl, [?] Three Mile Island, [?] and Fukushima [?]. While there are those that would debate that these examples are unfair representations [?], it is nevertheless true that

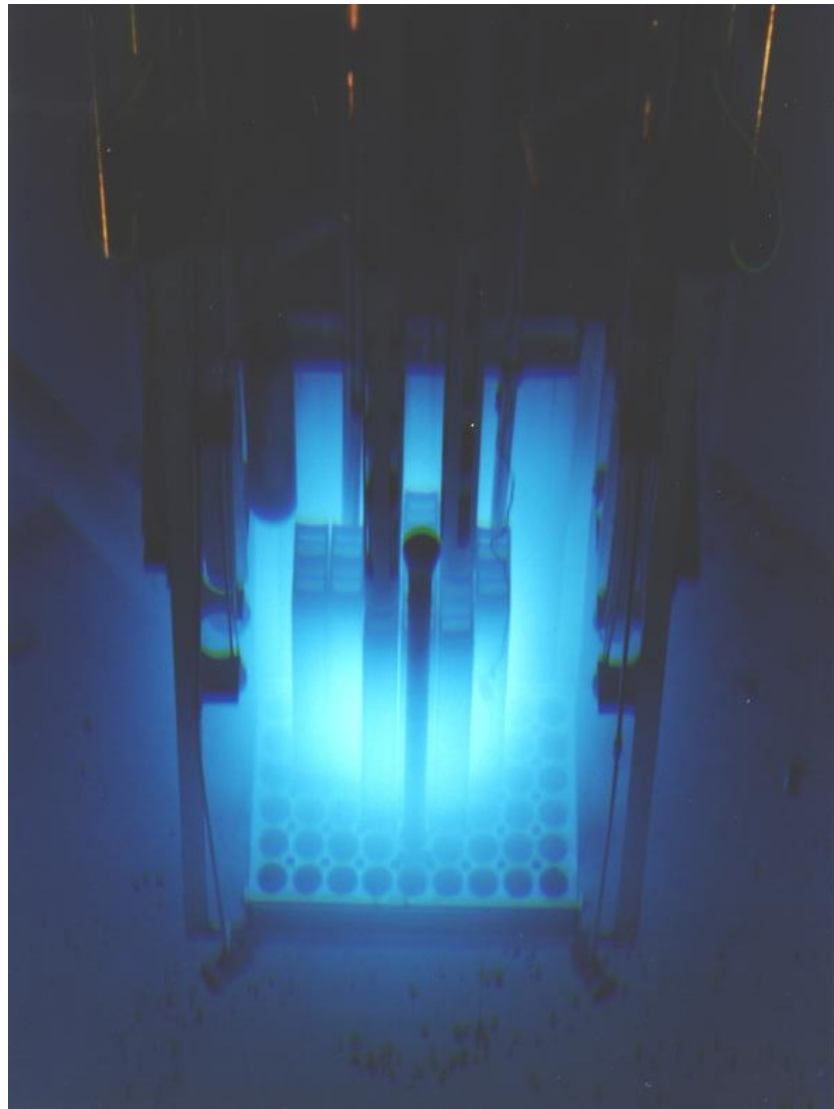


Figure 1-4: Nuclear reactor core of the Missouri University of Science & Technology Reactor (MSTR). The reactor generates 200 kW of thermal energy and is used primarily for research purposes. The blue glow comes from Cherenkov radiation, caused by high energy electrons being emitted from the fuel with speeds faster than light can travel in water. [? ?]

public opinion continues to be a challenge for nuclear fission. Another disadvantage of this technology is the spent fuel is a extreme radiation hazard have half lives on the order of millions of years. [?] While this spent fuel, as of yet, doesn't impact the environment, there is currently no long term plan in the United States on how to handle it. [?]

As noted before, the capital costs of nuclear fission power are much greater than

any other energy source. [?] Additionally, the act of getting a reactor approved and built is rather lengthy, full of complications, and prone to delays. [?] This significantly limits the number of potential investors who can or even who are willing to explore nuclear power. This makes expansion fundamentally difficult.

Another disadvantage is nuclear fission is (by many accounts) not a true renewable energy source. [?] The current most common and cheapest fuel cycles are extremely wasteful. The uranium must be enriched, so only about 10% of uranium mined out of the ground makes it into the reactor. Of this, roughly 5% is actually utilized for fission before becoming spent fuel. [?] Uranium resources used this way at current consumption rates can last on the order of hundreds of years. [?] In reality, there are other more efficient fuel cycles that can extend our resources to several thousand years but these come with costs and risks that are beyond the scope of this discussion. [?]

One final disadvantage is the concept of nuclear proliferation which, in this context, refers to the idea of a rogue and/or unstable organization acquiring nuclear weapon material somewhere in the fuel cycle. [?] In the wasteful cycle we mentioned before, this risk is fairly minimal. However, any efforts to reprocess spent fuel to more efficiently utilize it inherently involves the separation and concentration of plutonium. [?] Extreme care must be taken to ensure that none of this plutonium is diverted from the fuel cycle which presents a very real and challenging risk.

In conclusion, nuclear fission power holds extreme promise as an expandable base load power source that does not emit CO₂. It does, however, come with a vast amount of non trivial challenges. It certainly will play an important role in any carbon free energy profile, so long as the challenges can be appropriately addressed.

Nuclear Fusion

Nuclear fusion is very similar to nuclear fission except it involves combining light atoms (masses of order 1 amu) together. [?] Like with fission, this generates enormous amounts of energy which could be used as a heat source in any variety of thermodynamic cycles. Unlike with the other technologies discussed thus far, nuclear

fusion power has yet to be scientifically demonstrated. [?]

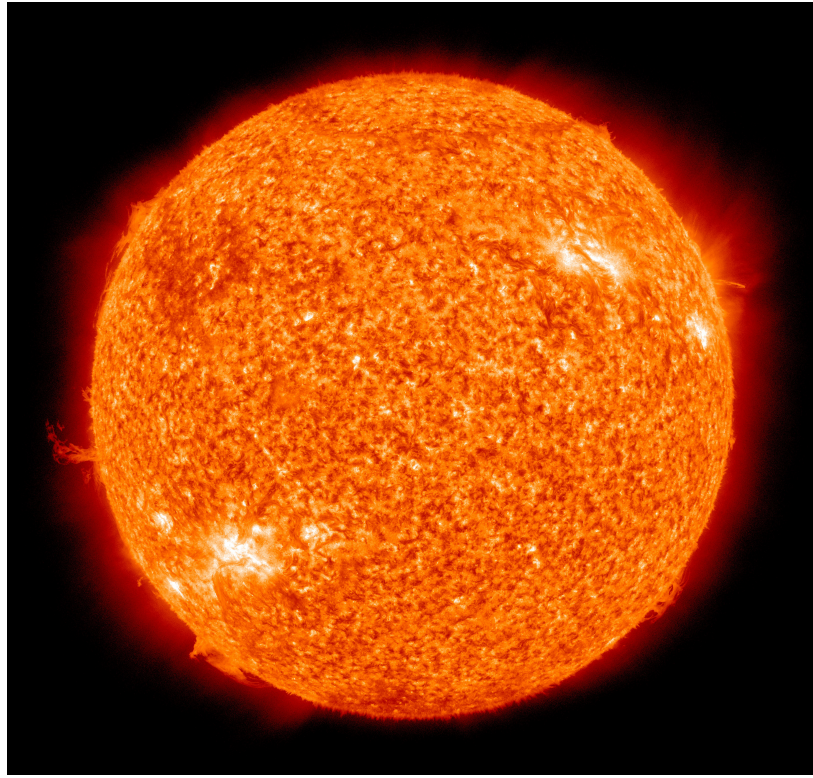


Figure 1-5: False-color image of the Sun taken at 304 angstroms. It is the star at the center of the Solar System. The Sun's power comes from the nuclear fusion of hydrogen atoms forced to extreme temperatures and pressures due to the Sun's own gravity. [? ?]

Nuclear fusion shares many of the advantages of nuclear fission. Like fission, nuclear fusion power would emit no CO₂ into the environment and it has an extremely high fuel energy density. If one were to consider the fusion of hydrogen isotopes tritium (T) and deuterium (D), the energy density is of order 3.5 MeV per amu compared to fission of ²³⁵U which is more like 0.85 MeV per amu. [?] It's also possible to simply fuse D with D which is found in trace amounts in water (H₂O). With this in mind, a perhaps more fair comparison is the potential fusion energy density of H₂O which is roughly 3×10^3 MJ/kg; still orders of magnitude above coal and methane. [?]

Like hinted at, the primary source of fuel for any nuclear fusion power scheme would be hydrogen. There are other reactions that would involve other fuels such

as helium or even boron, but we shall ignore those for now. [?] Deuterium is naturally present in water of which there is a significant abundance on Earth. [?] Any fusion power plant that used deuterium alone would certainly be considered effectively renewable due to the massive water reserves available in oceans. In reality, the first generation of nuclear fusion reactors would rely on tritium which does not exist naturally on Earth. It can, however, be produced from ^6Li or even deuterium via neutron bombardment. [?] Thankfully, lithium is also plentiful on Earth, not so much as to be considered renewable, but enough that it could last tens of thousands of years at current electrical consumption rates. [?]

A unique advantage of nuclear fusion is its intrinsic safety. The reason fusion power has yet to be scientifically demonstrated is exactly the same thing that makes it so safe. Nuclear fusion requires the containment of fuel hotter than the center of the Sun, which is an extreme scientific and engineering challenge. [?] While this may sound unsafe, it means that these extreme temperatures must be maintained for the fusion reaction to continue. Any failure mode that would result in a compromised containment which would immediately halt any additional fusion reactions. In addition, by design, fusion reactors only have very small amounts of fuel in the "core" at any given time. This is distinctly different from fission where a reactor is loaded with enough fuel such that 5% of it will last 18 months. [?]. What this means is that even if all of the fusion fuel were to be consumed in a runaway reaction, the total energy released would be minimal. In Inertial Confinement Fusion (ICF) schemes, all of the fuel in current designs translates to roughly 100 sticks of dynamite which is certainly containable with modern containment structures. [?]

Another advantage that nuclear fusion would have over nuclear fission, is the lack of long lived radioactive spent fuel. For fusion, the spent fuel is generally some combination of hydrogen and helium both of which are completely inert to the environment. [?] In the case of DD fusion, the spent fuel would actually be radioactive (in the form of tritium), but the half-life is on the order of 10 years, not millions. [?] Nuclear fusion does emit high energy neutrons that would go on to activate structural materials. These activated structural materials would have half-lives on the order of

hundreds of years, again much lower than that of spent fuel from nuclear fission. [?]

The primary disadvantage of nuclear fusion is quite clear; the technology does not exist. Unlike with nuclear fission power, nuclear fusion power has been out of reach for nearly 70 years. [?] This is because the technical demands associated with trying to contain a plasma hotter than the Sun here on Earth is quite challenging. To date, the technical viability of fusion has never been demonstrated outside of nuclear weapons and, in fact, many attempts have failed. [?] All of that said, the performance of nuclear fusion experiments has shown a steady increase over time suggesting that success will come inevitably. [?]

Another very real disadvantage of nuclear fusion is the expected costs. Nuclear fusion facilities are currently very expensive to operate and would never be able to generate electricity competitively. [?] For example, the National Ignition Facility (NIF) spends roughly **one million USD** per experiment. [?] The maximum theoretical yield from one of these experiments would generate less than 6 USD worth of electricity at current costs. [?] Using instead the maximum credible yield combined with the fact that energy will be lost converting to electricity brings this estimate below 1 USD. [?] While technology will be expected to lower costs over time and electricity prices are likely to rise, the fact remains that the current gap is many orders of magnitude away.

In summary nuclear fusion power holds great potential as a future base load power source with seemingly no safety risk or negative consequences. Its potential is locked entirely by technical and scientific issues that require more study and research. While nuclear fission is certainly sufficient to supply the World's clean energy needs in years to come, the vast potential of nuclear fusion justifies its continued investigation. We will therefore spend the introduction of this thesis discussing the basic theory and the current state of nuclear fusion efforts.

1.1 Physics of Nuclear Energy

The energy released from any reaction is dictated by Einstein's famous equation: [?]
]

$$E = mc^2 \quad (1.1)$$

where E is the so called rest mass energy of an object with mass m and c is the speed of light. To calculate the energy release of a reaction, one simply subtracts the rest mass energy of the initial state from the final state such that:

$$\Delta E \equiv Q = \left(\sum m_i - \sum m_f \right) c^2 \quad (1.2)$$

Here m_i is the masses of any initial components (particles in our context) and m_f is the masses of any final components. It is a common misconception that equation 1.2 only applies to nuclear reactions, but in reality chemical reactions are described by the same physics. Some example reactions are shown in Table 1.1.

Table 1.1: Mass differences and energy released by various reactions

Reaction	Type	$(\sum m_i - \sum m_f)$	Q
$p + e^- \rightarrow {}^1H$	Recombination	1.46×10^{-8} amu	13.6 eV
$n + {}^{235}U \rightarrow {}^{140}Xe + {}^{94}Sr + 2n$	Fission	0.198 amu	184.7 MeV
${}^2H + {}^3H \rightarrow {}^4He + n$	Fusion	0.0189 amu	17.6 MeV

For us to produce energy, we ultimately seek to find reactions that produce large Q . To do this we need reactants with large m_i relative to the m_f of the products. To aid in determining this, the masses of several isotopes are shown plotted in Figure 1-6.

As we can see, the isotope with the smallest mass per nuclide is ${}^{56}Fe$. It is considered the most efficiently bound nuclide since its corresponding rest mass energy per nuclide is lower than any other isotope. This means that for any isotopes lighter than ${}^{56}Fe$, we can gain energy by combining them (fusion) into heavier isotopes. Similarly, we gain energy by breaking up isotopes (fission) with mass greater than

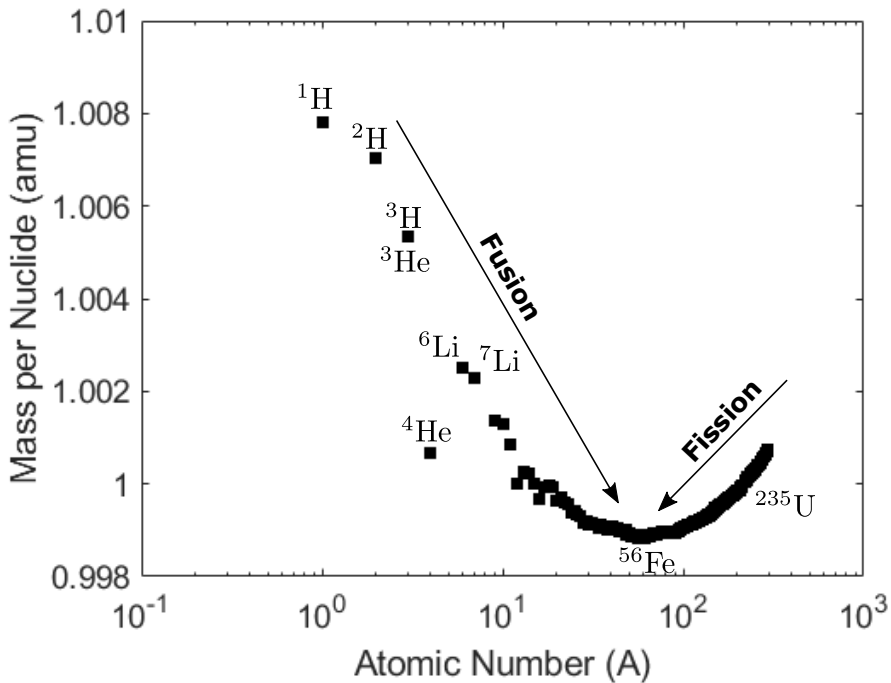


Figure 1-6: Mass per nuclide of various isotopes. All exothermic fusion reactions must occur between isotopes lighter than ^{56}Fe and all exothermic fission reactions must occur between isotopes heavier than ^{56}Fe .

^{56}Fe . It is interesting to note the local minimum mass per nuclide of ^4He . Due to its unique position, fusion reactions that produce it will be particularly energetic. Interestingly, it also means that the fission of ^6Li is uniquely exothermic. The exact reason for why isotope masses behave in this way is a topic of nuclear physics beyond the scope of this discussion.

Moving forward, we will adopt short-hand notations for a few light isotopes of particular interest to fusion. These isotopes are listed in Table 1.2.

Table 1.2: Short hand notations for a few light isotopes of particular interest to nuclear fusion

Name	Proper Notation	Short Hand
Deuteron	^2H	D
Triton	^3T	T
Alpha Particle	^4He	α

With this notation in mind, there are a few fusion reactions that are of particular

interest for energy production.



These reactions are primarily chosen due to the availability of the reactants, the amount of energy released, and the ease to which they can be made to fuse. The last of these criteria is described by the reaction's fusion cross-section (σ). Cross sections are essentially the probability (normalized for density and path length) that two particles will interact, or in our case fuse. As such, the cross section determines the reaction rate between two species. Formally the volumetric reaction rate between species 1 and 2 is given by:

$$\mathcal{R}_{12} = \int dv_1^3 \int dv_2^3 f_1(\vec{v}_1) f_2(\vec{v}_2) \sigma_{12} |\vec{v}_1 - \vec{v}_2| \quad (1.8)$$

where f_1 and f_2 are the velocity distribution functions of species 1 and 2 respectively and \vec{v}_1 and \vec{v}_2 are the velocities of species 1 and 2 respectively. The cross sections for all of the listed reactions are shown in Figure 1-7.

As we can see there are many orders of magnitude separating the cross-sections of these reactions depending on the center of mass energy. DT fusion (equation 1.5), is by far the easiest to achieve having a max cross section of about 5 barns. For context this is roughly 100 times less than the thermal fission cross section of ${}^{235}\text{U}$. Following DT, DD fusion (equations 1.3 and 1.4) is the next easiest to achieve at reasonable energies. For this reason, most major fusion experiments in the world aim for DT fusion as this will be the reaction that powers the first generation of nuclear fusion reactors. The other reactions listed have their advantages such as higher fuel

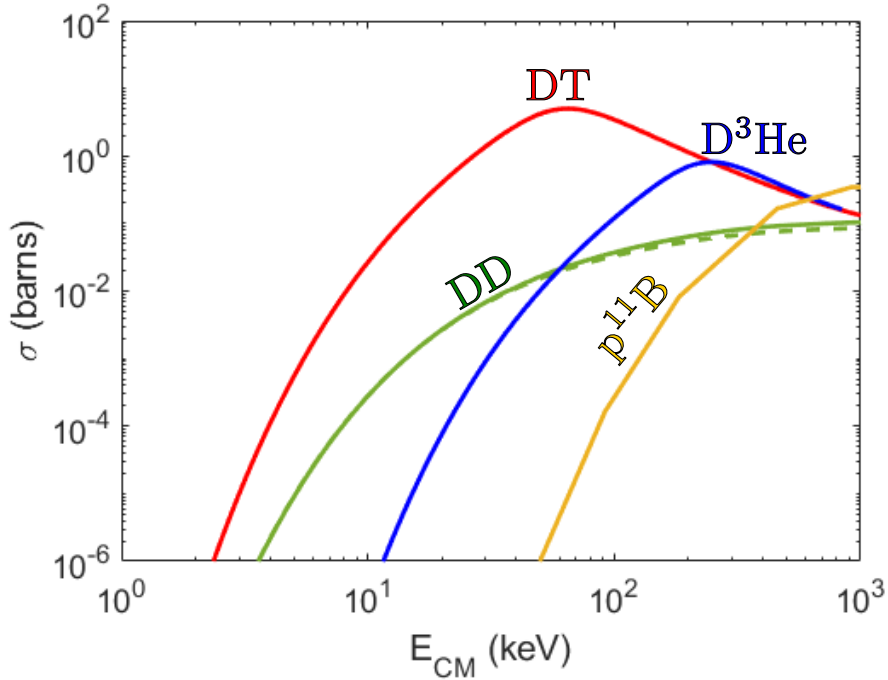


Figure 1-7: Cross sections of various fusion reactions consider for fusion energy. The cross sections for equations 1.3 - 1.7 are shown as green, green, red, blue, and yellow curves respectively. The cross sections for equations 1.3 and 1.4 are nearly identical up until very high energies. Equation 1.3 is dashed and equation 1.4 is solid. Cross sections here are plotted as a function of their center of mass energies.

availability or being aneutronic (emitting no neutrons) but will be reserved for second or third generation fusion reactors.

An important thing to note about these cross sections is the rather high center of mass energies required to achieve them. For reference, the fission cross section quoted previously occurs at room temperature energies (0.0253 eV) whereas the maximum DT cross section occurs at about 65 keV. This corresponds to temperatures of 750 million degrees Celsius (1.3 billion degrees Fahrenheit). This is because all fusion reactions require combining nuclides that are both positively charged leading to a Coulomb repulsion that can only be overcome with extreme energies. This Coulomb repulsion is also why the fusion of hydrogen atoms (who have the lowest possible charge) requires less energy than the reactions involving helium or boron. This is the primary challenge of nuclear fusion; creating and maintaining these extreme conditions.

Perhaps the most naive way to achieve nuclear fusion is through the acceleration of particles into a solid target. In fact this works remarkably well and is still the source of many fusion experiments to date. However, this approach to fusion is inefficient and cannot be used to generate net power. This is because the accelerated particle loses energy to Coulomb collisions with the solid target at a rate much higher than the fusion rate. A 100 keV triton, for example, travels less than 1 um into a solid target of pure deuterium before loosing all of its energy. This is compared to the 6000 um "mean fusion path length" one calculates from a 5 barn cross section. This means the fusion efficiency no better than 1/6000 (in fact it is much lower) but our energy gain per reaction is only 17.6 MeV / 100 keV = 176.

This necessitates thermonuclear fusion approaches, an approach in which the entire system is sufficiently heated to fusion viable temperatures. In a thermal system, internal Coulomb collisions are no longer a loss as they simply maintain the temperature. This is why most major approaches to fusion energy gain are thermonuclear. There are a few notable exceptions to this, but they're beyond the scope of this discussion.

The next question to address is, how hot does a thermonuclear system need to be in order to generate fusion power? To answer this we must return to equation 1.8 and replace f_1 and f_2 with thermal Maxwellian distributions.

$$\begin{aligned}\mathcal{R}_{12} &= \frac{n_1 n_2}{1 + \delta_{12}} \left(\frac{m_1 m_2}{4\pi^2 T_1 T_2} \right)^{3/2} \int dv_1^3 \int dv_2^3 e^{-\frac{m_1 |\vec{v}_1|^2}{2T_1}} e^{-\frac{m_2 |\vec{v}_2|^2}{2T_2}} \sigma_{12} |\vec{v}_1 - \vec{v}_2| \\ &= \frac{n_1 n_2}{1 + \delta_{12}} \langle \sigma v \rangle_{12}\end{aligned}\tag{1.9}$$

Here n_1 and n_2 are the number densities of species 1 and 2, δ_{12} is a Dirac delta to avoid double counting if species 1 and 2 are the same, m_1 and m_2 are the masses of species 1 and 2, and T_1 and T_2 are the temperatures (in units of energy) of species 1 and 2. Note that in the second line we have defined away the integrals into the term $\langle \sigma v \rangle_{12}$ which is called the *reactivity*. Note that this is very different than the concept of reactivity from nuclear fission. In nuclear fusion, reactivity is the density normalized reaction rate of species 1 and 2 at a given temperature. Reactivities for

all of the discussed reactions is shown in Figure 1-8.

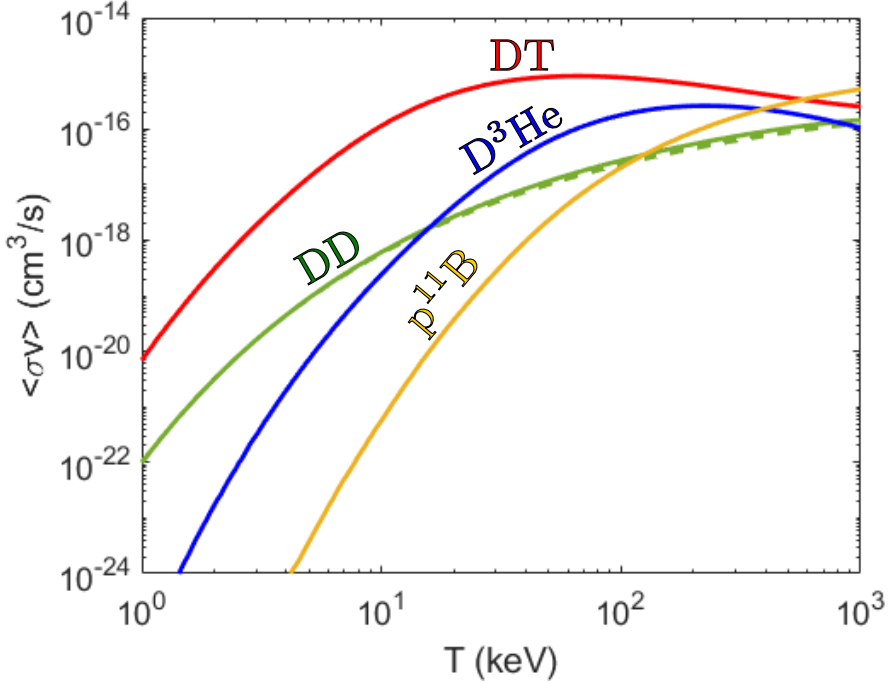


Figure 1-8: Reactivities of various fusion reactions considered for fusion energy. The reactivities for equations 1.3 - 1.7 are shown as green, green, red, blue, and yellow curves respectively. The reactivities for equations 1.3 and 1.4 are nearly identical up until very high temperatures. Equation 1.3 is dashed and equation 1.4 is solid.

1.2 Inertial Confinement Fusion

Traditionally, fusion power approaches aim to create plasma conditions hot enough to allow nuclear fusion and then maintain these conditions long enough (ideally indefinitely) to get a sufficient amount of power out. In these schemes, additional fuel is added to the system as fuel burns away without ever transitioning away from the desired plasma conditions.

Another approach is a pulsed scheme, one where a single component of fuel is brought to the desired temperature and density until all or most of it burns away. Instead of maintaining extreme plasma conditions, they would be recreated each time for each individual component of fuel. This process would be repeated at some

frequency in order to achieve some desired power output.

One immediate problem with this approach is the limited energy gain available. As we've seen from Figure 1-8, nuclear fusion requires temperatures of order 10 to 20 keV and the total energy received (for DT) is 17.6 MeV. Assume we expend some energy to create a DT plasma with $n_D = n_T = n/2$ and we burn some fraction f of the fuel. The fractional energy gain G would be:

$$G = \frac{E_{gain}}{E_{spent}} = \frac{fnQ}{3/2(n_D T + n_T T)} = \frac{Qf}{3T} \quad (1.10)$$

In the absolute best case scenario $f = 100\%$ and taking $T = 20$ keV, we achieve a gain of roughly 600. This may seem like a lot, but it's extremely limiting from an engineering standpoint as it represents the absolute best we can possibly do. Once you start to consider any realistic inefficiencies (40% from Carnot, 10% from the heating process, 50% fuel utilization, etc) the potential energy profit starts to diminish rapidly. This approach of heating the entire fuel volume is often referred to as *volume ignition*.

To get around this, we consider a hybrid approach that we'll refer to as *hot-spot ignition*. In this pulsed power approach, we will still only interact with a single fuel component at a time but we'll only heat some fraction of it to fusion conditions. The remaining *cold fuel* will be heated from the fusion power itself; specifically from the charged particle products. For DT fusion, this means that the α particles (which only carry 20% of the energy) will heat the remaining cold fuel. This creates a runaway process in the form of a propagating burn wave throughout the entire fuel volume. See Figure 1-9 for a diagram of this idea.

We only need the hot-spot to generate enough energy to heat up the cold fuel immediately around it. A detailed calculate of this is not entirely straightforward but let's say a factor of 2 more energy than what is required to heat it. Accounting for the fact that α s only carry 20% of the energy means we need a hot-spot G of about 10. This means we need to burn about $f_{HS} = 3\%$.

Let's consider now, how long it will take to burn away this fraction of fuel. Taking

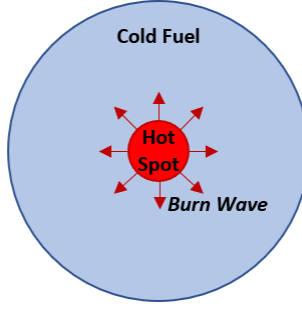


Figure 1-9: Cartoon of the hot-spot ignition scheme. Only a small fraction of the fuel is brought to fusion temperatures to begin the process. This hot-spot then initiates a *burn-wave* that propagates outward, heating the remaining fuel volume. This significantly reduces the total energy required to ignite the entire volume.

equation 1.9 we can write down the differential equation that governs rate of fuel burn:

$$\frac{dn}{dt} = -\frac{n^2}{2} \langle \sigma v \rangle_{DT} \quad (1.11)$$

Or in terms of f :

$$\frac{df}{dt} = (1 - f)^2 \frac{n_0}{2} \langle \sigma v \rangle_{DT} \quad (1.12)$$

where n_0 is the initial fill density of the fuel. If we assume $\langle \sigma v \rangle$ is roughly constant over the burn, we can solve for f to get:

$$f = \frac{n_0 \langle \sigma v \rangle_{DT} \tau}{2 + n_0 \langle \sigma v \rangle_{DT} \tau} \quad (1.13)$$

Where τ is the duration over which the fuel is able to burn.

As a side note, this equation is important because it highlights the three key components involved in burning fusion fuel; density (n_0), temperature ($\langle \sigma v \rangle$), and confinement time (τ). It is similar to (but not the same as) the Lawson criteria in this way. All approaches to fusion must raise some combination of these three factors high enough in order to efficiently produce fusion power. Often the difference between approaches come down to what factor is being focused.

For inertial confinement fusion (ICF), we seek to minimize the complications associated with confining these extreme condition plasmas. We do this by recognizing

that any plasma will take a finite amount of time to disassemble itself. If we can get the plasma to a final state that burns sufficiently fast, that finite amount of time will be sufficient. We have yet to discuss how we'll get the plasma to this state, but let's explore the requirements associated with trying to do that.

Without any confinement, a plasma will disassemble at a rate proportional to the acoustic ion sound speed:

$$c_s = \sqrt{\frac{4T}{m_{DT}}} \quad (1.14)$$

Here we have assumed the electrons have the same temperature (T_e) as the ions. The fuel will continue burning so long as the density of the fuel has not sufficiently changed. Let's assume our fuel is all contained in a sphere of radius R such that we can allow it to disassemble for some $\tau < R/c_s$ before the burn is too negatively effected. The exact value for τ is a bit arbitrary, and deserves detailed calculations, but most literature takes it to be $R/4c_s$. We can plug this into equation 1.13 to show:

$$\begin{aligned} f &= \frac{n_0 \langle \sigma v \rangle_{DT} R / 4c_s}{2 + n_0 \langle \sigma v \rangle_{DT} R / 4c_s} \\ &= \frac{n_0 m_{DT} R}{n_0 m_{DT} R + \frac{8c_s m_{DT}}{\langle \sigma v \rangle_{DT}}} \\ &= \frac{\rho R}{\rho R + H_B} \end{aligned} \quad (1.15)$$

Here we've defined a few new terms. ρR is the areal density of the plasma and H_B is the so called *burn parameter* which depends entirely on T . By defining our τ through the ICF approach, we have reduced our parameter space from three to two parameters. This means we can easily plot the fusion requirements for ICF schemes.

Using Figure 1-10 we can set some requirements for an ICF approach to achieve high gain. First we have the hot-spot ignition requirement from before of $f_{HS} = 3\%$ which corresponds to an areal density of roughly 0.3 g/cm^2 at temperatures around 20 keV. For the rest of the fuel assembly, we want burn fractions high enough to produce substantial gain, but low enough to minimize the areal density requirement. For now let's take $f = 30\%$ which corresponds to areal densities around $4-5 \text{ g/cm}^2$

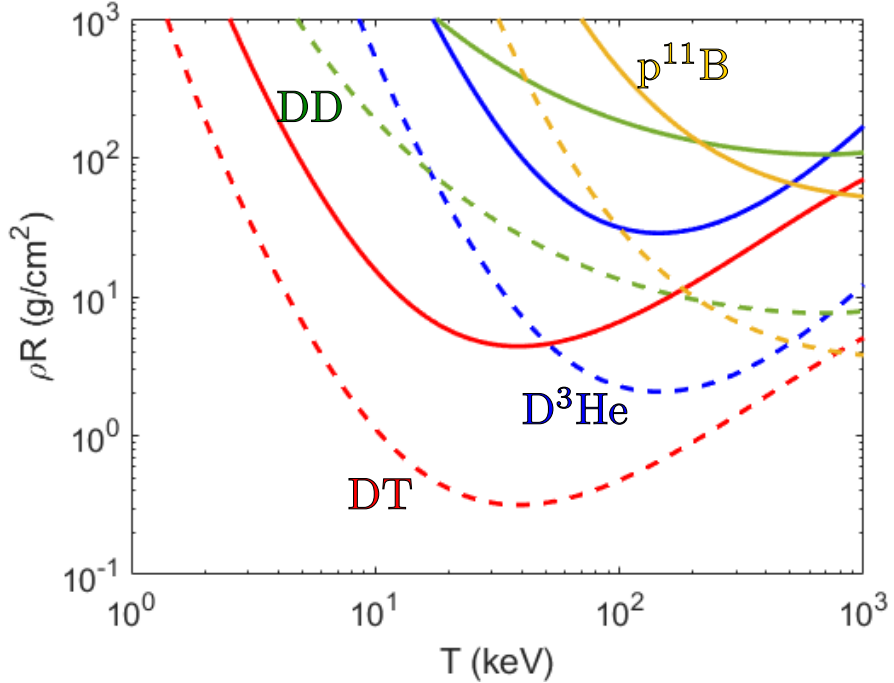


Figure 1-10: Areal density and temperature requirements to burn certain fuel fractions in ICF schemes. Dashed curves correspond to the hot-spot requirement of $f_{HS} = 3\%$ and solid curves correspond to a cold-fuel high gain requirement of $f = 30\%$. Different fuels are plotted as different colors. DT, D³He, DD, and p¹¹B are plotted as red, blue, green, and yellow respectively.

for DT fuels.

The next question to address is how to get these areal densities. The most naive way would be to construct a fuel assembly with R sufficiently large so as to meet the requirement. If we take the density of DT ice to be roughly 0.225 g/cm^3 we can achieve a ρR of 4.5 g/cm^2 with an $R = 20 \text{ cm}$. We can calculate the total energy released from this assembly:

$$\begin{aligned}
 E_{tot} &\sim \mathcal{R}_{12} \times \tau \times V \times f \times Q \\
 &\sim (n_D n_T \langle \sigma v \rangle_{DT}) \times \left(\frac{R}{4c_s} \right) \times \left(\frac{4}{3}\pi R^3 \right) \times \left(\frac{\rho R}{\rho R + H_B} \right) \times Q \\
 &\sim \frac{\pi \langle \sigma v \rangle_{DT}}{3m_{DT}^2 c_s} \left(\frac{\rho R}{\rho R + H_B} \right) Q (\rho R)^2 R^2
 \end{aligned} \tag{1.16}$$

Plugging in our numbers get us $E_{tot} \sim 5 \times 10^{14} \text{ J}$ or roughly 12 kT of TNT. Roughly

the yield from the Little Boy bomb dropped Hiroshima in 1945. While this is certainly an impressive yield of energy, it's not particularly conducive to our goal of designing a fusion reactor that doesn't detonate itself and the people around it. In order to ensure our reactor is safe and reasonable, we must put an additional constraint on E_{tot} . However, the only free parameter left in equation 1.16 is R . Rearranging the equation we get:

$$R = \frac{1}{\rho R} \sqrt{\left(\frac{3m_{DT}^2 c_s}{\pi \langle \sigma v \rangle_{DT}} \right) \left(\frac{\rho R + H_B}{\rho R} \right) \left(\frac{E_{tot}}{Q} \right)} \quad (1.17)$$

It's debatable what limit we can set for E_{tot} , but most sources seem to be of the order 100 MJ. Plugging in our numbers gets us a R of roughly 280 μm which makes the corresponding $\rho = 160 \text{ g/cm}^2$, which is roughly 700 times the solid density of the DT ice. So, in order to achieve reasonably low fusion energies (while still getting high gain) using an ICF scheme requires compressing DT fuel to extreme densities. In reality, the hot-spot generally starts as DT vapor for a variety of reasons and thus requires much more compression to reach its target areal density of 0.3 g/cm^2 . Ignition designs generally quote convergence ratios (the ratio between the initial and final radii) of 20-35.

Currently no discussion on shocks / how ignition temperature is achieved

There are a handful of methods that can be used to achieve this compression, but all major methods today use high power lasers. The basic idea is to start with a small hallow spherical target of DT ice surrounded by an ablator material. Various ablators have been considered including plastic, beryllium, and high-density carbon (diamond or HDC). The ablator material is rapidly and symmetrically heated by the laser causing it to expand outward and force the rest of the target inwards. This kind of *direct drive* of the target is the major approach being explored at the OMEGA laser Facility discussed in Section 1.4.2.

One of the hardest challenges of ICF is the symmetric compression of the fuel. Any asymmetries get severely amplified during the compression and risk tearing the fuel

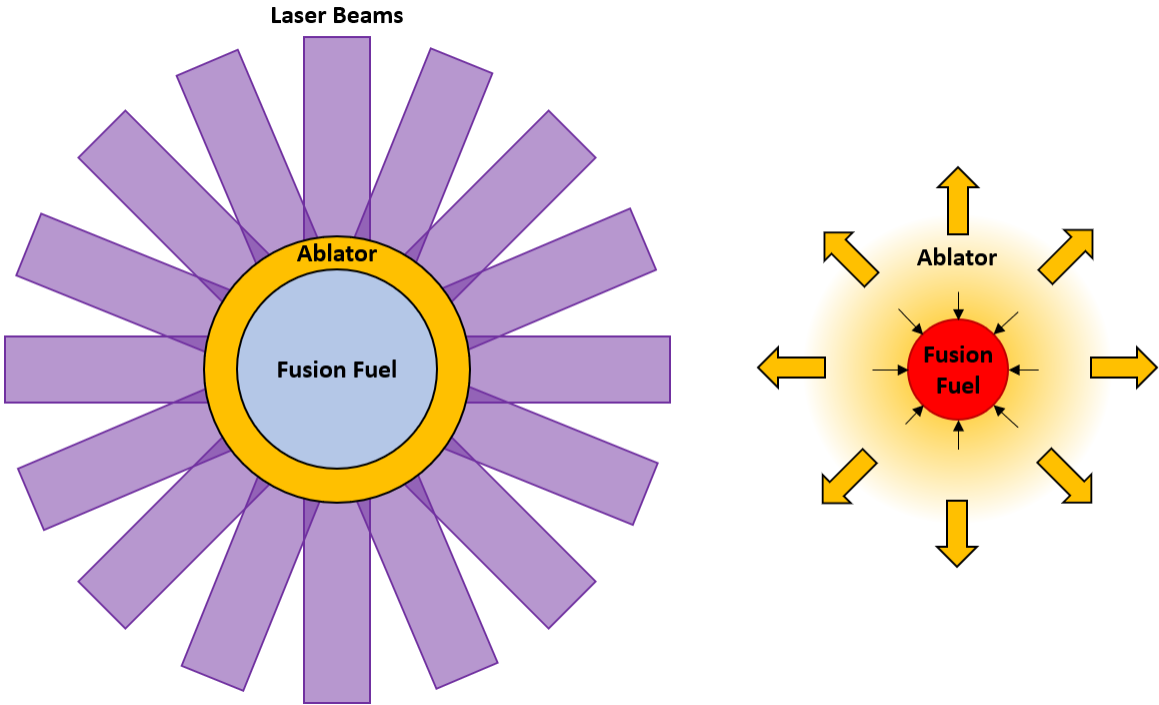


Figure 1-11: Schematic of laser direct drive. Lasers directly heat an ablation material that quickly expands outward, sending the fuel layer inward.

assembly apart before peak compression is reached. An alternative drive technique called *indirect drive* tries to improve symmetry by first heating the inside of a can referred to as a *hohlraum*. The hohlraum is made of a high Z material like gold or depleted-uranium and emits black-body radiation once it's heated. The x-rays from this emission then go on to heat the ablator which achieves compression exactly as described before. This approach to ICF is the main approach being explored at the National Ignition Facility (NIF) discussed in Section 1.4.4.

1.3 Magnetized Liner Inertial Fusion

Magnetized Liner Inertial Fusion (MagLIF) is an alternative approach to ICF fusion that takes advantage Z-pinch type confinement geometry. The MagLIF scheme sends intense currents axially up a cylindrical liner, generating a radial magnetic field which ultimately compresses the liner inward. This compression technology turns out to be significantly more efficient ($\sim 10\%$) than laser approaches ($\sim 1\%$) generally used in

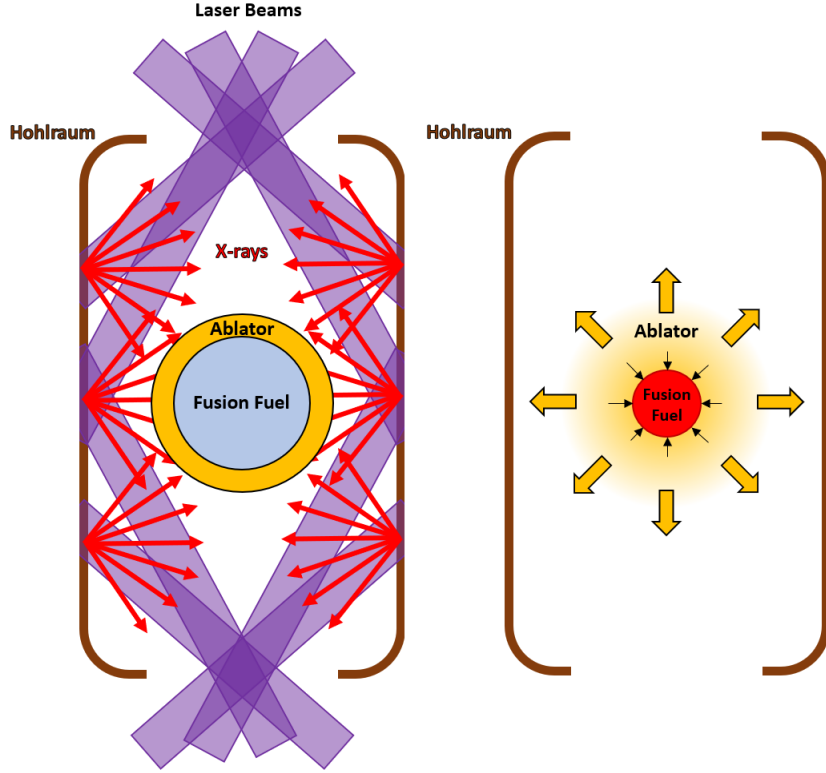


Figure 1-12: Schematic of laser indirect drive. Lasers heat the inside of a hohlraum causing it to symmetrically emit blackbody x-rays. These x-rays go on to heat the ablator material causing it to expand outward, sending the fuel layer inward. When compared to direct drive, indirect drive is thought to be more symmetric albeit less efficient.

ICF schemes. The liner contains DT fuel, that get compressed with the liner and ideally ignites. In addition to this compression, an external axial magnetic field is applied to aid in the confinement of the fuel. In this way, MagLIF acts as a hybrid like approach between magnetic confinement and inertial confinement fusion. This is the major approach being explored at the Z Pulsed Power Facility discussed in Section 1.4.3.

Figure 1-13: **Z-pinch or MagLIF**

The unique nature of this approach changes the ignition requirements considerably. First off, the liner is designed to survive the compression meaning it provides a "cage" of the final burning fuel. This constricts the expansion for the burning plasma and significantly increases the confinement time. We can get an estimate of this con-

finement by using Newton's second law to describe the burning plasma pressing on a thin liner

$$M_l \frac{d^2 R}{dt^2} = P_0(2\pi R) \quad (1.18)$$

where M_l is the mass per unit length of the liner, and P_0 is the pressure of the burning plasma. The characteristic time scale of this motion is the confinement time. It is given by:

$$\tau \propto \sqrt{M_l/(2\pi P_0)} \quad (1.19)$$

We can replace some of these values with terms that we are more familiar with:

$$\tau \propto \frac{\sqrt{R}}{c_s} \sqrt{\frac{\rho_L t_L}{\rho}} \quad (1.20)$$

where $\rho_L t_L$ is the areal density of the liner. Plugging this new confinement time into equation 1.15 gives us:

$$f = \frac{\sqrt{\rho R \rho_L t_L}}{\sqrt{\rho R \rho_L t_L} + H_B} \quad (1.21)$$

Here we've just assumed the same 1/4 pre-factor as before for convenience. Note that the true burn fraction requires much more sophisticated simulations. Despite that though, this equation illustrates the advantage of the liner in reducing the required fuel areal density. Based on this scaling, a linear areal density of 5 mg/cm² reduces the required hot-spot areal density to 0.02 g/cm². This significantly reduces the required compression.

One disadvantage of this reduced areal density requirement is the confinement of the alpha particles. One happy coincidence of the ICF requirement of 0.3 g/cm² is that's approximately the range of a 3.5 MeV alpha particle. With only 0.02 g/cm², the alpha particles will freely stream into the liner without depositing their heat back into the hot-spot. The remedy for this is the external magnetic field. While this isn't the sole reason for the externally applied magnetic field, it does solve this problem by magnetically confining the alpha particles that travel radially. In order to accomplish this, the gyro radius of the alpha particles, must be of the order of the system radius:

$$\begin{aligned} R/R_\alpha &> 1 \\ BR &> 26.5 \text{ Tesla-cm} \end{aligned} \tag{1.22}$$

Here R_α is the gyro radius of a 3.5 MeV alpha particle, and B is the axial magnetic field strength at peak compression.

Of course, no such confinement exists axially so the areal density must be sufficiently large on axis. To ensure this we take:

$$\rho H = 0.5 \text{ g/cm}^2 \tag{1.23}$$

where H is the height of the liner.

Due to constraints that are beyond the scope of this discussion, this final hot-spot density needs to be of order 1 g/cm³. This means we require a final radius of $R = 200 \mu\text{m}$, a height of $H = 1.0 \text{ cm}$ and a final magnetic field strength of over 1000 Tesla. This may seem unmanageable at first but the magnetic fields get compressed with the liner meaning our initial magnetic field strength can be much lower. A starting DT gas density of 5 mg/cc would imply convergences of the order of 15 which correspond to an initial magnetic field strength as low as 6 Tesla.

One last thing that should be noted is the fact that ignition temperatures cannot be reached by the slow cylindrical implosions that we have described. To get around this, MagLIF makes an additional alteration to the ICF scheme by preheating the fuel before it is compressed. This is done via a laser that penetrates the fuel from the top. See Figure 1-13 for a depiction of this.

Table comparing implosion parameters?

1.4 Experimental Facilities

1.4.1 MIT High Energy Density Physics (HEDP) Accelerator Facility

The MIT High Energy Density Physics (HEDP) Accelerator Facility is a laboratory at MIT used by the HEDP group led by Richard Petrasso. Its primary experimental facility is the Linear Electrostatic Ion Accelerator (LEIA) used for the development of nuclear diagnostics. The accelerator has an ion source from which deuterium or helium-3 ions can be accelerated up to energies of 135 keV. The beamline leads to a large cylindrical target chamber that has an erbium deuteride target located in the center. The accelerator is capable of producing roughly 10^7 DD fusion products per second and roughly 10^6 D³He fusion products per second.

Figure 1-14: Accelerator

The accelerator has a charged-particle detection system that uses Surface Barrier Detectors (SBDs). These are used to calibrate and develop various nuclear diagnostics. The machine was built and is maintained and operated largely by students in the program. All the work discussed within this thesis can trace some dependence back to this facility. Some work that depended exclusively on this facility are highlighted in [list Appendixes ...](#)

1.4.2 The OMEGA Laser Facility

The OMEGA Laser Facility is a 60 beam laser capable of delivering 30 kJ at 60 TW of ultraviolet light onto targets less than 1 millimeter in diameter. The laser is located in Rochester, NY and operated by the Laboratory for Laser Energetics (LLE). All the beams are delivered symmetrically to a 130 in diameter target chamber. The target chamber is kept under vacuum at under 5×10^{-7} Torr. The OMEGA laser has a vast array of diagnostic systems that are either fixed to the target chamber or inserted

manually during each shot. The facility is capable of firing the laser once every 45 minutes and can perform roughly 12-14 experiments per standard day of operations.

Figure 1-15: OMEGA Laser

The OMEGA laser was used for the Warm Dense Matter (WDM) stopping power experiments described in Chapter ??.

1.4.3 The Z Pulsed Power Facility

The Z Pulsed Power Facility (informally known as the Z-machine or the Z) is the world's largest Z-pinch located in Albuquerque, NM operated by Sandia National Laboratories. It consists of 36 Marx Bank Generators that form a circle roughly 33 meters in diameter. Each have sixty 2.6 uF capacitors that are charged in parallel and discharged in series. Each generator can be discharged to generate a 150 kA current within 1.5 microseconds. The current travels through a series of intermediate capacitors that ultimately compress and combine the pulses to deliver currents between 10 to 26 MA with durations between 100 to 1000 ns. This facility is used for a vast variety of different experiments, but in our context, the current is delivered to a small cylindrical liner in the center of the machine.

Figure 1-16: Z Machine

The Z Pulsed Power facility was used for the experiments described in Chapter ???. The diagnostic discussed here was specifically made for the Z facility and will continue to see use beyond the work of this thesis.

1.4.4 The National Ignition Facility

The National Ignition Facility (NIF) is the world's most powerful laser located in Livermore, CA operated by Lawrence Livermore National Laboratory (LLNL). The NIF is an 192 beam laser capable of delivering 1.8 MJ at 500 TW. The beams are delivered through the top and bottom of a 10 meter diameter target chamber as

opposed to the symmetric layout of the OMEGA laser. This is because the NIF is designed for the indirect drive approach to ICF discussed in Section 1.2. Like the OMEGA facility, the NIF is equipped with a vast array of diagnostics that are either fixed to the target chamber or inserted prior to a shot.

The work discussed in Chapter 2 comes from a variety of experiments performed at the NIF.

2 | Secondary DT Neutron Measurements on the NIF

2.1 Secondary Nuclear Reactions

2.1.1 Introduction

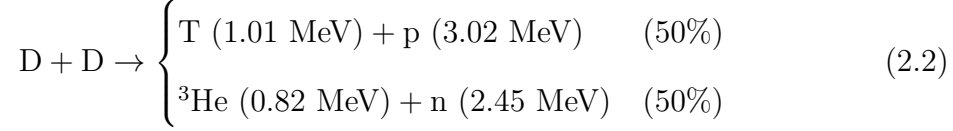
Nuclear fusion almost always produces highly energized nuclear particles that can, themselves, undergo nuclear fusion. In fact, these products are often more suited for nuclear fusion than their thermal parents due to their high birth energies. In general:

$$Q/T_{ion} \sim 10^3 \quad (2.1)$$

Where Q is the energy generated in a nuclear reaction and T_{ion} is the ion temperature of a typical burning plasma. This process is conceptually not too different than the fission concept of *chain-reactions* whereby neutrons from fission will go on to generate more fission reactions with some efficiency. As we will see however, this process is much less efficient in the case of nuclear fusion.

When these highly energized products go on to generate their own nuclear reaction, the event is referred to as a *secondary nuclear reaction*. It should be noted that the reactions of interest occur between the products and thermal plasma from whence they came, as opposed to between a pair of products. The latter is significantly less likely to occur simply due to the density of the thermal plasma being several orders of magnitude above the density of the fusion products.

For an example of this, consider the two primary fusion reactions of a pure deuterium plasma:



All four of these products can go on to have their own secondary nuclear reactions within the deuterium plasma. Scattering reactions in the case of the neutrons, and fusion reactions in case of the other three products. The triton, for example, can go on to have the following secondary reaction:



We note that the energy width of these products in the lab frame are significantly higher than typical broadening seen from thermal nuclear reactions ($\Delta E_{DTn} \sim 400$ keV for a 5 keV DT plasma). This, again, is due to the significantly higher center-of-mass energy present in secondary reactions. Appendix A covers the details on calculating these energy ranges.

2.1.2 Yield Ratios

One measurable of interest is the yield of these secondary nuclear reactions. In general, it is simply:

$$Y_2 = Y_1 \times \langle \mathbb{P}_{12} \rangle \quad (2.4)$$

where Y_1 is the yield of the primary reaction and \mathbb{P}_{12} is the probability of a given primary product undergoing a secondary nuclear reaction. This probability is given by:

$$\mathbb{P}_{12} = 1 - \exp \left[- \int d\ell n_j \sigma_{ij} \right] \quad (2.5)$$

where $d\ell$ is the path length element of the primary product i , n_j is the density of the background ion species j , and σ_{ij} is the cross section of the secondary nuclear reaction. In the case of secondary DT fusion, n_j would be n_D and σ_{ij} would be σ_{DT} .

In general, the integral in equation 2.5 is $\ll 1$, meaning we can Taylor expand it such that:

$$\mathbb{P}_{12} \sim \int d\ell n_j \sigma_{ij} \quad (2.6)$$

which when combined with equation 2.4 implies:

$$\left(\frac{Y_2}{Y_1} \right) \sim \left\langle \int d\ell n_j \sigma_{ij} \right\rangle \quad (2.7)$$

As the primary product streams through the plasma, it will continuously lose energy to Coulomb collisions at a rate described by its local stopping power $(\frac{dE}{dp_x})$. As a result, σ_{ij} changes value throughout the path integral. The rate of this energy loss as well as how it impacts σ_{ij} is shown in Figure 2-1 for a couple of secondary nuclear reactions.

Figure 2-1: Energy and fusion cross sections of primary products as they stream through a deuterium plasma with a temperature of 5 keV and a density of 1 g/cc. The solid lines track the properties of a DD triton and its probability of undergoing DT fusion and the dashed lines track the properties of a DD helium-3 ion and its probability of undergoing D³He fusion. Blue curves represent the corresponding cross section and red curves represent the corresponding energy.

If the areal density (ρR) of the plasma is sufficiently small, the primary product will stream through the entire plasma in a straight line losing a minimal amount of energy. In this case, σ_{ij} is roughly constant and the path of the secondary particle will be of order R , the radius of the plasma. As a result:

$$\left(\frac{Y_2}{Y_1} \right) \propto \langle \rho R \rangle_j \quad (2.8)$$

in this regime. If, alternatively, the areal density is sufficiently high, the secondary particle will not be able to escape the plasma. Instead it will lose all of its energy to Coulomb collisions and become thermalized with the plasma. In this process, σ_{ij} will effectively tend to 0 and the yield ratio will asymptote to a fixed value. In other

words:

$$\left(\frac{Y_2}{Y_1}\right) \sim \text{constant} \quad (2.9)$$

in this regime. Figure 2-2 shows the simulated behavior of the yield ratio as a function of ρR for a couple secondary nuclear reactions.

Figure 2-2: Yield ratio of secondary DT reactions (red) and secondary D³He reactions (blue) to their corresponding primary DD reactions. The solid, dashed, and dash-dotted curves correspond to plasma source with temperature equal 8.0, 4.0, and 2.0 keV respectively. For low areal densities, yield ratios are proportional to the areal density and for high areal densities, the yield ratios asymptote to a constant value. The exact saturation value varies with plasma properties such as T_e (illustrated here) and n_e . The transition region between the two extremes exist due to the secondary particles having non mono energetic spectra and volumetric birth profiles. These curves were generated using the Monte Carlo model discussed in [where?](#). The source plasma was deuterium filled will a uniform 1.0 g/cc density and uniform temperature. Primary product particles were sampled from the corresponding (uniform) DD burn distribution.

The exact saturation point and value of the yield ratios depends on how much areal density is required to thermalize the primary product in question. This, again, is described by the stopping power of the plasma on said particle. The details of plasma stopping power is itself an entire research topic, but for the purposes of this work it is sufficient to know that it is a strong function of the plasma's electron temperature (T_e) and electron density (n_e). This means, the saturation points of the yield ratios are themselves a strong function of these parameters. It is important to note, that this dependency only manifests at moderate to high areal densities, that is areal densities of the order of the primary product's maximum range. Below this point, the yield ratio depends only on the areal density of the plasma and is agnostic to other plasma parameters. The behavior is also shown in Figure 2-2.

These characteristics make the yield ratio of secondary reactions a strong diagnostic tool for integrated plasma conditions. [More](#)

2.1.3 Secondary Spectra

As mentioned, secondary reactions create particles with an enormous range of energies due to the high center of mass energy of the reaction. An example of this is the secondary DT reaction given by equation 2.3. More specifically, the different lab energies correspond to the direction the primary product particle was traveling relative to the observer. The exact dependence is shown in equation A.11. This is also shown plotted in the case of secondary DT neutrons in Figure 2-3.

Figure 2-3: Relationship between the lab angle θ and the resulting energy of a secondary DT neutron. The red, blue, and green curves show the case of a 1.0, 0.6, and 0.2 MeV triton resulting in the birth of the neutron. The black dashed line corresponds to the so called *zero-temperature birth energy* of a DT neutron; the case when both parents have exactly 0 energy. While technically θ in equation A.11 refers to the angle between the triton and the neutron, the angle between the line of sight and the triton is almost exactly equal for any detector any reasonable distance away from the plasma.

As the primary product loses energy in the source plasma, the secondary particle's energy-angle relationship changes. Notably the centroid shifts, and the range of energies becomes narrower. In cases where a significant amount of energy is loss, the resulting spectra will be a convolution of these different relationships. Some example spectra are shown in Figure 2-4

Figure 2-4: Resulting secondary DT neutron spectra from deuterium source plasmas of varying areal densities. Simulations used a uniform density and temperature of 1.0 g/cc and 4 keV respectively. The red, blue, and green curve correspond to areal densities of 20, 60, and 100 mg/cm². As the areal density increases to and beyond the average range of a 1.01 MeV triton, the spectra gets more narrow and the centroid shifts to lower energies. Like the yield ratio, this behavior has a threshold to it. All spectra below approximately 20 mg/cm² look identical to one another and all spectra above 100 mg/cm² look identical as well.

This relationship between lab angle and secondary product energy, means the shape of a measured secondary spectra encode the shape of the source plasma relative to the detector. For low areal density plasmas, every energy uniquely maps to a angle

about the detector line of sight. This means that the secondary yield ratio between a given energy bin E to $E + \Delta E$ is a measurement of an azimuthally averaged areal density between angles $\theta(E)$ and $\theta(E + \Delta E)$. For higher areal density plasmas, ranging creates a degeneracy between energy and angle which makes the relationship less clear, but the dependence remains. Examples of spectra from asymmetric plasma sources is shown in Figure 2-5.

Figure 2-5: Simulated secondary DT neutron spectra from prolate deuterium plasma sources with uniform density and uniform temperature 1.0 g/cc and 4.0 keV respectively. The red (blue) curves are the secondary spectra as measured from the equator (pole). The dashed and solid curves correspond to an average areal density of 10 mg/cm² and 100 mg/cm² respectively. The spectral shapes map out the areal density asymmetry relative to their respective lines of sight. Different lines of sight measure different spectra due to their orientations relative to the asymmetries. [list \$R\(\theta\)\$](#)

2.2 Simulating Secondary Nuclear Reactions

Secondary reactions integrate over a significant amount of information by their nature. In general, the primary product is born from a time-evolving spatially-varying plasma source. This alone creates complication, but it must further probe these varying plasma conditions as it streams through the plasma. The secondary particle ultimately depends on the state of the primary product at fusion which is influenced by all of these factors.

These complications motivate a model capable of creating and simulating the life of these primary products. Without simplification, the problem has $N = 7$ dimensions; spatial position, velocity, and time. This motivates using a Monte Carlo approach to avoid the curse of dimensionality.

2.2.1 Monte Carlo Model for Tracing Particles Through a Plasma

A model has been created for creating and tracing arbitrary particles through arbitrary plasma conditions. This model is useful for many applications, but for our purposes can be used to generate secondary nuclear reactions by tracing primary nuclear products through a given plasma source. As of the writing of this thesis, the full code can be found at <https://github.com/bLahmann/MonteCarloParticleTracer>.

In this model, a plasma is defined by several parameters. The first is the outer radius bound:

$$R_o(\theta, \varphi) = \sum_{\ell=0}^{\infty} \sum_{m=-\ell}^{\ell} (\Delta_o)_\ell^m \alpha_\ell^m \cos(m\varphi) P_\ell^m(\cos \theta) \quad (2.10)$$

where $(\Delta_o)_\ell^m$ are user-provided outer magnitudes (set equal to 0 if unspecified), α_ℓ^m is a normalization factor given by:

$$\alpha_\ell^m = \sqrt{\frac{2\ell+1}{4\pi} \frac{(\ell-m)!}{(\ell+m)!}} \quad (2.11)$$

and P_ℓ^m is an associated Legendre polynomials. Similarly, an inner radius bound is specified as:

$$R_i(\theta, \varphi) = \sum_{\ell=0}^{\infty} \sum_{m=-\ell}^{\ell} (\Delta_i)_\ell^m \alpha_\ell^m \cos(m\varphi) P_\ell^m(\cos \theta) \quad (2.12)$$

where $(\Delta_i)_\ell^m$ are user-provided inner magnitudes (set equal to 0 if unspecified). Plasma properties between the bounds are specified on a normalized radial grid $\hat{r}(r, \theta, \varphi) \in [0, 1]$ defined by:

$$\hat{r}(r, \theta, \varphi) = \frac{r - R_i(\theta, \varphi)}{R_o(\theta, \varphi) - R_i(\theta, \varphi)} \quad (2.13)$$

The plasma properties are fully defined by a radial mass density $\rho(\hat{r})$, a radial ion temperature $T_{ion}(\hat{r})$, and a radial electron temperature $T_e(\hat{r})$. These are specified by the user as double arrays evaluated at user-specified points on the normalized radius

grid. Finally, the plasma consists of an arbitrary number (>0) of plasma ion species. These are specified as a list of particle types (defined by their charges $\{Z_j\}$ and masses $\{M_j\}$) and a list of their corresponding number proportions $\{f_j\}$ defined as:

$$f_j = \frac{n_j(\hat{r})}{n(\hat{r})} \quad (2.14)$$

where n_j is the number density of ion species j and n is the total number density.

In this simplified specification model, a few key assumptions have been made. First is the separability of the plasma profiles. As specified, all profiles can only belong to a set of separable functions such that:

$$\mathcal{F}(r, \theta, \varphi) = \mathcal{R}(r)\mathcal{G}(\theta, \varphi) \quad (2.15)$$

This assumption is made purely out of convenience as has no theoretical basis. The second assumption is that all plasma ion species have the same ion temperature profile $T_{ion}(\hat{r})$. That is, all ion species are always in thermal equilibrium. Finally we have assumed that number proportions $\{f_j\}$ are all constant throughout space. This disallows any ion-separation type modeling.

The model requires that at least one plasma be fully specified. Additional plasmas can be added in *layers* if desired. The model stacks these plasmas by forcing the inner boundary of every additional layer to be equal to the outer boundary of the layer before it.

Additionally the model requires that the user specify a particle source. The particle source is assumed to be born within the first specified plasma layer. The source is specified with a viable nuclear reaction (one that can occur between the plasma ion species in plasma layer) and a radial source distribution $N_{source}(\hat{r})$. Like plasma profiles this is defined with an array of doubles specifying the evaluated source density at specified values of \hat{r} . Alternatively, the user can provide a reactivity table $\langle\sigma v\rangle_{source}(T_{ion})$ and the source profile will be automatically specified as:

$$N_{source}(\hat{r}) \propto \hat{r}^2 \rho(\hat{r})^2 \langle\sigma v\rangle_{source}(T_{ion}(\hat{r})) \quad (2.16)$$

While this information is sufficient for useful models to be run, additional information needs to be provided for secondary particle calculations. The model allows for an arbitrary number of nuclear reactions to be tracked in the simulation. To simulate secondary reactions, the appropriate secondary nuclear reaction (one that can occur between the source particle and ion species within specified plasma layers) needs to be specified. All nuclear reactions are specified by a list of reactant particle types, (specified by Z and M), a list of product particle types, as well as a cross section table $\sigma(E_{COM})$, where E_{COM} is the center of mass energy of the reaction.

The library comes with several pre-specified objects such as plasmas and nuclear reactions to aid in model specification. An example full specification routine using the Java API is shown in Figure 2-6.

Each simulation consists of N_p particles which can be distributed across N_{CPU} number of processors specified by the user. Particles have their positions sampled from the specified radial source distribution and a polar distribution given by:

$$f(\theta, \varphi) \propto \sin \theta (R_o(\theta, \varphi) - R_i(\theta, \varphi)) \quad (2.17)$$

Their direction of travel are sampled randomly from a uniform spherical distribution and their energies are sampled from a normal distribution:

$$f(E) = \mathcal{N} \left(\frac{m_D}{m_C + m_D} Q, \quad \frac{2m_C m_D}{(m_A + m_B)(m_C + m_D)} Q T_{ion}(\vec{r}_0) \right) \quad (2.18)$$

Where m_A , m_B , m_C and m_D are the masses specified in the source nuclear reaction, Q is the energy gain of the specified source nuclear reaction, and $T_{ion}(\vec{r}_0)$ is the ion temperature evaluated at the birth position. Note that this formulation does not include up-shifts in the mean energy caused by the non-zero local temperature of the plasma. [?] This approximation is thought to be more than sufficient for secondary particle applications although a more exact implementation would not require a great

```

import MonteCarloParticleTracer.*;

public class ExampleSetup {

    public static void main(String ... args) {

        // *****
        // Plasma information *
        // *****

        // Uniform profiles
        double[] rhat = new double[]{0.0, 0.5, 1.0};           // Normalized units
        double[] rho = new double[]{1.0, 1.0, 1.0};           // Units g/cc
        double[] Tion = new double[]{4.0, 4.0, 4.0};          // Units keV
        double[] Te = new double[]{4.0, 4.0, 4.0};            // Units in keV

        // Outer radius information
        // Here we're setting an l=0 and l=2 mode
        int[] ells = new int[]{0, 2};
        int[] ms = new int[]{0, 0};
        double[] magnitudes = new double[]{50 * 1e-4, 0.1 * 50 * 1e-4};

        // *****
        // Source information *
        // *****

        // Prebuilt DDp reactivity table
        Reactivity sourceReactivity = Reactivity.DDp_Reactivity;

        // Prebuilt D+D->T+p reaction
        NuclearReaction sourceReaction = NuclearReaction.DD_t;

        // Prebuilt D+T->n+a nuclear reaction
        NuclearReaction secondaryDTn = NuclearReaction.DT_n;

        // *****
        // Build the simulation *
        // *****

        // Create the plasma object
        Plasma plasma = new Plasma(rhat, Tion, Te, rho);
        plasma.addSpecies(ParticleType.deuteron, 1.0);
        for (int i = 0; i < magnitudes.length; i++) {
            plasma.addOuterLegendreMode(ells[i], ms[i], magnitudes[i]);
        }

        // Create the model
        Model model = new Model("Example_Model");
        model.addPlasmaLayer(plasma);
        model.setSourceInformation(sourceReaction, sourceReactivity);
        model.addNuclearReaction(secondaryDTn);

        // Run the model
        model.runSimulation((int) 1e6, 20);

    }
}

```

Figure 2-6: Example setup of the Monte Carlo Particle Tracer routine. In this simulation, the user has specified a deuterium plasma with uniform density and temperatures of 1.0 g/cc and 4.0 keV respectively. The plasma is a prolate spheroid and the source particles being traced are DD tritons. DT neutron reactions have been added to the model to simulate secondary DT neutrons resulting from the triton tracing.

deal of work. All source particles are born with a weight:

$$w_{source} = \frac{1}{N_p} \quad (2.19)$$

Particles then take steps through their current plasma layer until they reach a boundary or they lose all of their energy. The length of any given step is given by:

$$\delta x_j = \frac{\min \left[L, \frac{E_0}{(dE/dx)_j} \right]}{N_{STEPS}} \quad (2.20)$$

Where L is the distance between the starting position and plasma layer boundary, E_0 is the birth energy of the particle being traced, $(dE/dx)_j$ is the local stopping power of the particle with the plasma layer evaluated at it's current position, and N_{STEPS} is a hard coded integer set sufficiently large to resolve the plasma but sufficiently small so as to minimize computation time. Current implementations take $N_{STEPS} = 50$. This flexible step length ensures smaller steps are taken to resolve details when dE/dx is large. Future implementations may also want to have step sizes based on profile gradients as well to ensure profile information is resolved when gradients are sharp.

It should be noted that calculating L for any given position \vec{r} and direction $\vec{\Omega}$ is itself a non-trivial calculation. Additionally, it must be computed several times ($\mathcal{O}(N_p \times N_{STEPS})$ for secondary calculations) so the calculation must be computationally efficient. Currently, the model uses a bisection method approach with the initial guess being:

$$L_0 = \left(R_o(\vec{\Omega}) - R_i(\vec{\Omega}) \right) \quad (2.21)$$

One problem with this method, is it is not guaranteed to return the smallest solution if there are more than one. In other words, the method fails for concave boundaries. One way to fix this is to simply choose L_0 sufficiently small ($\sim \delta x$) to correctly resolve any concavities in the plasma. Unfortunately, this causes noticeably large increases in computation time due to the increased iteration requirement of the bisection method. Finding a more elegant solution to this problem would be of great

benefit to the simulation algorithm.

With every step, a variety of routines are performed. The particles position is updated based on the step size, the particles energy is updated based on the local plasma stopping power, and a nuclear particle is born for every viable nuclear reaction added to the simulation. These product particles are born at the position of their parent with weight equal to:

$$w_{product} = w_{parent} \mathbb{P}_j \quad (2.22)$$

where w_{parent} is equal to the weight of the parent particle and \mathbb{P}_j is the probability of the parent particle having a nuclear reaction during the current step given by:

$$\mathbb{P}_j = n_j \sigma_j \delta x_j (1 - \mathbb{P}_{tot}) \quad (2.23)$$

where n_j is the average number density of the reacting species evaluated over this step, σ_j is the average cross section between the traced particle and the reacting plasma species evaluated over this step, and \mathbb{P}_{tot} is the running total reaction probability for this particle given by:

$$\mathbb{P}_{tot} = \sum_{k=0}^j \mathbb{P}_k \quad (2.24)$$

To determine the value of σ_j , a background particle is sampled from the appropriate plasma species. It's direction is sampled from a random spherical distribution and it's energy is sampled from a Maxwell distribution:

$$f(E) \propto \sqrt{E} \exp\left[-\frac{E}{T_{ion}(\hat{r})}\right] \quad (2.25)$$

The energy of the product particle is given by:

$$E_C = \frac{1}{2} m_C |\vec{v}_C|^2 \quad (2.26)$$

where \vec{v}_C is the lab frame velocity and this time m_C is the mass of the product particle from the specified nuclear reaction. Note that the product nuclear reaction

is not necessarily equivalent to the source nuclear reaction. The lab frame velocity is given by:

$$\vec{v}_C = \vec{u}_C + \vec{v}_{CM} \quad (2.27)$$

where \vec{u}_C is the center of mass velocity of the product particle and v_{CM} is the system's center of mass velocity given by:

$$\vec{v}_{CM} = \frac{m_A \vec{v}_A + m_B \vec{v}_B}{m_A + m_B} \quad (2.28)$$

Where m_A and \vec{v}_A are the mass and velocity of the background particle and m_B and \vec{v}_B are the mass and velocity of the traced particle. The magnitude of \vec{u}_C is given by:

$$|\vec{u}_C| = \sqrt{\frac{2\mathcal{E}_C}{m_C}} \quad (2.29)$$

where \mathcal{E}_C is the center-of-mass energy of the product particle given by:

$$\mathcal{E}_C = \frac{m_D}{m_C + m_D} (Q + K) \quad (2.30)$$

where Q is the energy gain of the product reaction given by:

$$Q = (m_A + m_B - m_C - m_D) c^2 \quad (2.31)$$

where c is the speed of light, and K is the kinetic energy given by:

$$K = \frac{1}{2} \mu (\vec{v}_A - \vec{v}_B)^2 \quad (2.32)$$

and μ is the reduced mass given by:

$$\mu = \frac{m_A m_B}{m_A + m_B} \quad (2.33)$$

In default operations, \vec{u}_C is sampled randomly from a uniform spherical distribution. In reality, the direction should be sampled from the differential cross section ($\frac{d\sigma_j}{d\Omega}$) but this feature is not currently implemented. Such details are not important for

the secondary reactions discussed in this work because the differential cross section is nearly uniform. However, such details are required for other applications such as *knock-on deuterons* [?] that make adding this feature in the future desirable.

Alternatively, the user can specify the direction of \vec{v}_C (such that products only go to a detector of interest) when setting up the model. In this case, it is possible to calculate the magnitude of \vec{v}_C without knowing the direction of \vec{u}_C by using the law of cosines:

$$|\vec{u}_C|^2 = |\vec{v}_C|^2 + |\vec{v}_{CM}|^2 - 2(\vec{v}_C \cdot \vec{v}_{CM}) \quad (2.34)$$

It is important to note that forcing the direction like this, results in non-physical distributions of \vec{u}_C . To correct this bias, the weight of the product particle needs to be multiplied by a correction term: [?]

$$w_{product}^* = w_{product} \left(\frac{E_C}{\mathcal{E}_C} \right) \quad (2.35)$$

This correction term is, in itself, an approximation to the real correction. While the approximation holds for $|\vec{v}_C| \gg |\vec{v}_B|$, implementing the correct term would not require a great deal of additional work.

After having it's direction and energy set, the parent particle routine pauses and the product particle begins tracing through the plasma. This process continues recursively until all of the original N_p particles are traced.

We take a moment to note that every single particle produces on the order of N_{STEPS} secondary particles instead of the more physical case of $\sim n\sigma R$. This is valid because we are weighting the products according to the probability that they could have existed. This approach is useful because $n\sigma R \ll 1$ meaning we would have to sample many source particles just to tally a single secondary reaction. With the current algorithm, meaningful spectra can be produced with N_p as low as 10^4 .

2.2.2 Profile Effects

With the model, we can investigate the impact that temperature and density profiles have on the observables. There are a handful of common models we can use to do this. The first commonly used model is the *Hot Spot Model*. In this model temperature and densities are taken to be uniform throughout the plasma. Instead of following the burn distribution, all particles are born at the center of the plasma. That is:

$$N_{source}(\hat{r}) = \delta_r(0); \quad (2.36)$$

where δ_r is the Dirac delta function. Every other model discussed will use equation 2.16 to describe the source birth profile.

All models we consider (including the Hot Spot Model) have a temperature profile such that:

$$T_{ion}(\hat{r}) = T_e(\hat{r}) \propto (1 - \hat{r}^2)^\gamma \quad (2.37)$$

where γ is just some exponent describing the peakedness of the profile. When $\gamma = 0$, the model is referred to as the *Uniform Model* because the temperature profiles are uniform.

The magnitude of the temperature profiles is set by the burn averaged temperature given by:

$$\langle T \rangle_{burn} = \frac{\int_V dV \rho^2 \langle \sigma v \rangle_{source} T_{ion}}{\int_V dV \rho^2 \langle \sigma v \rangle_{source}} \quad (2.38)$$

Yield Ratios

Spectra

2.2.3 Asymmetry Effects

Yield Ratios

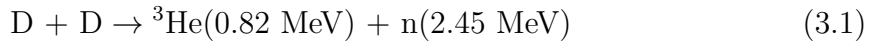
Spectra

2.3 Measuring Secondaries on the NIF

References

3 | title

Deuterium gas (D_2) filled Inertial Confinement Fusion (ICF) implosions are routinely executed at the National Ignition Facility (NIF) [?], the OMEGA laser [?], and the Z facility [?]. In these experiments, fusion neutrons are generated via the following reaction:



The spectra of these neutrons carry information on several metrics that relate to fusion performance. The total number (or yield Y_{DDn}) of neutrons is a fully integrated measurement of performance and the most common metric quoted when judging the success of an experiment. Additionally, the temperature of the burning plasma (T_{DDn}) can be inferred from the Doppler-broadened DD neutron spectra. [?] Finally the areal density (ρR) of an implosion can be inferred by measuring the fraction of neutrons that have scattered down in energy while escaping the plasma. In practice, the number is often directly quoted as a down-scatter ratio (dsr) [? ?].

Y_{DDn} , T_{DDn} , and ρR all have thresholds that must be met in order to achieve ignition. [?] For this reason, the NIF, OMEGA, and the Z facility all use neutron time of flight (nToF) spectrometers to measure DD neutron spectra [? ? ? ?]. For any of these measurements to be accurate, neutron scattering from the environment or experimental setup must be well understood and accounted for. In practice, extensive Monte Carlo models of the experimental facility are used to predict the impact of scattering. In cases where scattering is significant, any uncertainties in these models and/or the experimental geometry can dominate the total uncertain-

ties on any inferred value. This is of particular importance at the Z facility where neutrons scattering off the massive amount of hardware surrounding the implosion greatly complicate the interpretation of the nToF data.

For these reasons, it is valuable to have alternative diagnostics for measuring DD neutron spectra. Complementary diagnostics not only reduce the total uncertainty on the measurement, but also provide means for validating the required Monte Carlo models. One potential diagnostic is a CR-39 based recoil spectrometer. CR-39 is a solid-state detector with moderate sensitivity to DD neutrons (of order 10^{-5} to 10^{-4}) and a demonstrated robustness to intense electromagnetic pulses (EMP) very common in ICF environments. [?] It is also already routinely fielded for charged-particle and neutron spectroscopy at the NIF and OMEGA [? ? ? ? ? ? ? ? ? ?].

The structure of this paper is as follows. Section 3.1 explains the basic concepts and design parameters governing the CR-39 based recoil-spectrometer. Section 3.2 shows the first CR-39 based DD neutron spectrum measurement on the Z facility using a basic proof-of-principle design. Section 3.3 discusses the full optimization and theoretical performance of an improved shielded spectrometer.

3.1 Basic Conceptual Design

When a neutron elastically scatters off an ion, the resultant recoil-ion will have an energy of:

$$E_A = \frac{4A}{(1+A)^2} E_n \cos^2 \theta \quad (3.2)$$

where A is the atomic mass of the ion, E_n is the incident energy of the neutron, and θ is the lab-frame angle between the incident neutron and the outgoing recoil-ion. This means, for some fixed angle, there is a fixed relationship between the recoil-ion-energies and the neutron-energies. Neutron recoil-spectrometers take advantage of this mechanism by using a thin “conversion foil” for neutrons to scatter in and a charged-particle spectrometer some distance away. An illustration of design concepts are shown in Figure 3-1.

Figure 3-1: Illustrations of two concepts for a DD-n spectrometer. In each case, incoming neutrons pass through a conversion foil in which some of them have elastic collisions with ions. Many of the recoil ions are knocked in the general direction of a CR-39 detector, where their spectrum can be measured and converted to a spectrum of the incident neutrons. Figure 3-1a depicts the most simple design with the conversion foil directly in line with the detector. This minimizes θ and thus maximizes E_A . Additionally, it requires the smallest possible footprint. Figure 3-1b shows a design with an annular conversion foil. This leaves space in-front of the detector free for things like shielding or structure components. Shielding requirements are discussed in more detail in Section 3.3.

Using the most basic example in Figure 3-1a, there are three main parameters that define the recoil-spectrometer: the distance between the conversion foil and neutron-source (ℓ_s), the distance between the conversion-foil and detector (ℓ_d), and the thickness of the conversion-foil (t_f). As ℓ_s and ℓ_d are minimized, the total number of recoil-ions detected is increased. However, this also decreases energy resolution as a greater range of θ values will land on the detector. Similarly, maximizing t_f also increases the total number of recoil ions but decreases energy resolution due to ions losing energy to Coulomb collisions within the foil itself. These effects were quantified using MCNP6 [?] for the case of a CH₂ foil and are shown in Figure 3-2. Examples of simulated recoil-proton spectra are shown in Figure 3-3.

Figure 3-2: Contours of the total number of protons per cm² per 10¹² DD neutrons (a) and the signal full-width-half-max in keV (b) as a function of the detector distance (ℓ_d) and the foil thickness (t_f). The simulations assumed a mono-energetic 2.5 MeV neutron source, a 5.0 cm diameter for the foil and detector, and a neutron-source distance (ℓ_s) of 30.0 cm. The foil was made of 1.0 g/cm³ of CH₂ and the recoil-ions were protons.

Figure 3-3: MCNP6-simulated recoil-proton spectra from the data-set plotted in Figure 3-2. The red diamond (blue square) data is for the case $\ell_d = 50$ (10) cm and $t_f = 20$ (1) μm . Effectively, the two spectra demonstrate the broadening associated with thick filters and small distances respectively.

Figure 3-2b shows that energy resolution decreases with filter thickness in a linear and predictable manner. By contrast, the detector distance has a threshold like

behavior being non-consequential above distances of 15 cm. The detection efficiency is roughly linear with foil thickness and quadratic with inverse detector distance as would be expected.

The exact values needed are application dependent. Z routinely produces DD_n yields of the order 10^{12} , meaning the entire parameter space plotted in Figure 3-2 would be sufficient for a measurement of Y_{DD_n} . The full-width-half-max of a neutron spectrum emitted from a 2 (4) keV deuterium plasma is 115 (165) keV, meaning foil thicknesses of 10 μm or less must be used for a temperature measurement. However, there is an intrinsic 330 keV full-width-half-max broadening associated with current analysis techniques of CR-39 detectors that is not considered in Figure 3-2. [?] As a result, a temperature measurement would be impossible with a CR-39-based spectrometer. This also means that using foil thicknesses less than 25 μm does not benefit to a CR-39 based spectrometer.

Determining the dsr measurement quality requires more care and is more explicitly modeled in Section 3.3. However, one can get rough approximations by simply multiplying the desired dsr by the values in Figure 3-2a. For example, for a dsr of 1% one might expect anywhere from 1 to 100 recoil-protons per cm^2 per $10^{12} Y_{DD_n}$ from down-scattered neutrons.

3.2 Proof-of-Principle Design

To test the concept on the Z facility, a simple neutron recoil-spectrometer with the design depicted in Figure 3-1a was built and subsequently fielded. A detailed model of the spectrometer is shown in Figure 3-4.

Figure 3-4: SOLIDWORKS drawing of the neutron recoil-spectrometer fielded on the Z facility for shot z3135. The spectrometer consisted of a CH₂ conversion foil (yellow) and CR-39 detector (teal) all contained within an aluminum tube (gray) housing structure. The foil was 10 μm thick and positioned 25 cm away from the CR-39 detector. These parameters were chosen in an attempt to measure the ion temperature. This was done before the CR-39 broadening was well characterized.

The spectrometer was fielded on shot z3135, with the front of the housing sitting

approximately 30 cm away from target chamber center (TCC). Because the spectrometer was not shielded, the recoil-proton signal to neutron background was of order 0.2. The coincidence counting technique (CCT) [? ?] was used to reject most of the neutron background, increasing the ratio to 1.9. The resulting spectrum is shown in Figure 3-5.

Figure 3-5: DDn spectrum from shot z3135, measured by the proof-of-principle neutron recoil-spectrometer shown in Figure 3-4. The spectrum was determined from the CR-39 detector after using CCT to reduce the neutron background. The red data points are the raw data and the black dashed curve is a Gaussian fit to the main peak. The yield under the Gaussian is between 1.7×10^{12} and 2.8×10^{12} depending on the modeling of the scattering environment. The yield as inferred by indium activation was roughly 3.0×10^{12} . The FWHM of the Gaussian fit was 528 keV.

The FWHM of the peak was 528 keV, which is well beyond any width that would be caused by temperature broadening. This is partly because the CR-39 was processed in such a way that the FWHM of response would have been 425 ± 50 keV. When combined in quadrature with the broadening from Figure 3-2 this increases slightly to 440 ± 50 keV. The remaining broadening is likely from neutron-scattering not properly captured in the instrument response function (IRF).

As mentioned in Section ??, the inferred yield is strongly dependent on the modeling of the scattering environment. If only the spectrometer is modeled, the inferred yield is 1.7×10^{12} . If a scattering environment is included, the inferred yield is 2.8×10^{12} which is in good agreement with the indium-activation inferred value of $3.0 \pm 0.6 \times 10^{12}$. This gives confidence to the understanding of this spectrometer.

Despite some flaws in the measurement, the proof-of-principle design demonstrated that a CR-39-based neutron-recoil-spectrometer can be fielded on the Z facility. It also demonstrated the need for neutron shielding and the significance of external neutron-scattering sources.

3.3 Shielded Annular Foil Design

Because inferring the plasma temperature from the DD neutron spectrum is not feasible with current CR-39 analysis techniques, the recoil-spectrometer design has been optimized for the dsr measurement. To do this, the dsr signal to background ($(S/B)_{dsr}$) needs to be maximized. It is given by:

$$\left(\frac{S}{B}\right)_{dsr} = \frac{\int_{E_{\min}}^{E_{dsr}} dE (\phi_p^{\text{liner}} - \phi_p^{\text{no-liner}})}{\int_{E_{\min}}^{E_{dsr}} dE \phi_p^{\text{no-liner}} + \int_{E_{\min}}^{\infty} dE \eta_n \phi_n^{\text{liner}}} \quad (3.3)$$

where ϕ_p^{liner} and $\phi_p^{\text{no-liner}}$ are the recoil-proton fluences at the detector for the case of a compressed liner and no liner respectively, ϕ_n^{liner} is the neutron fluence at the detector for the case of a compressed liner, η_n is the CR-39 efficiency to neutrons, E_{\min} is the minimum energy for which CR-39 can detect protons, and E_{dsr} is the maximum energy for which down-scattered recoil-protons dominate the proton spectrum. It should be noted that this equation assumes that $\phi_p^{\text{no-liner}}$ represents the component of ϕ_p^{liner} that has not interacted with the liner, which is not strictly true.

The primary control we have on this equation is through the ϕ_n^{liner} integral, which can be minimized by the addition of neutron shielding. The design discussed in Section 3.2 cannot accommodate shielding because the conversion foil is in-line with the detector. Instead, the shielded recoil-spectrometer design will use an annular conversion foil similar to the concept shown in Figure 3-1b. A detailed schematic of the proposed design is shown in Figure 3-6.

Figure 3-6: SOLIDWORKS drawing of the neutron-recoil-spectrometer proposed for the Z facility. The CR-39 detector (teal) is shielded from direct line-of-sight neutrons by a polyethylene plug (red) directly in front. The conversion foil (yellow) is annular and separated from shielding plug by a thin sheet of aluminum. This prevents recoil-protons created within the shield from reaching the CR-39 detector. The whole system is contained within an aluminum housing (gray) which is itself surrounded by a layer of polyethylene (blue) to shield again external neutron scatter sources. The outer surface of the aluminum housing is conical with respect to TCC so as to reduce the amount of neutron-scatter caused by the spectrometer itself.

3.3.1 Internal Shielding

The CR-39 detector is shielded from direct line of sight neutrons using a polyethylene plug between the neutron source and the detector. The plug is a truncated cone with a slope that, if extended, would intersect at the TCC. It is important that the shield plug be separated from the detector to prevent inadvertently measuring recoil-protons from the shield-plug. In theory, this only requires 80 (30) μm of Al (Ta), but thicker materials would likely be required for structural integrity. The exact length of the internal-shielding plug was determined using MCNP6 to calculate $(S/B)_{dsr}$ from equation 3.3. The results of this calculation for several plug lengths is shown in Figure 3-7.

Figure 3-7: MCNP6 integrated down-scattered proton fluences in the case of a compressed liner (blue squares), in the case of no liner (yellow circles), and neutron-induced protons in the CR-39 (red diamonds) for various lengths of shield plugs. Figure 3-7(a) illustrates the cases where the housing was not modeled and Figure 3-7(b) illustrates the cases where the housing was modeled. Both figures do not model the external shield nor any additional sources of external scattering. In these calculations, the compressed liners had an areal density of 1.3 g/cm^2 and all other parameters were taken from Table 3.3. Both Figures show $(S/B)_{dsr}$ plotted as black dashed curves.

Figure 3-7a shows that the neutron background is effectively eliminated with a 20 cm polyethylene plug when the housing material is not considered. However, Figure 3-7b shows that neutrons that scatter off the housing begin to dominate once the housing is modeled. This scattering primarily comes from the mid plate that separates the detector and shield plug due to its direct line of sight with the neutron-source and its proximity to the detector. For this reason, it's important that this thickness be minimized as much as possible. $(S/B)_{dsr}$ reaches a value of approximately 5 if the shield length is extended to 50 cm using a mid-plate of 100 μm of aluminum.

3.3.2 External Shielding

In addition to self-scatter in the spectrometer housing, there are several sources of neutron scattering external to the system on the Z facility. These external scattering sources allow neutrons to reach the detector via paths that don't intersect the internal shield plug. These neutrons can further increase background if unmitigated. In this study, three sources of external scattering are considered: a titanium spacer that separates the magnetic coils, a steel blast-shield, and the Magnetically Insulated Transmission Line (MITL) deck that the spectrometer is attached to. These were all simplified and modeled in MCNP6 as hollow cylinders with dimensions shown in Table 3.1. In the model, the blast shield has a rectangular line of sight (LOS) hole in line with the detector. This modeling over-estimates the effects of scattering since all of these components are much more complicated with many additional holes created for diagnostics. A much more accurate SOLIDWORKS model of these components is shown in Figure 3-8.

Figure 3-8: SOLIDWORKS model of an example line-of-sight that a neutron-recoil-spectrometer might have at the Z facility. Of particular interest is the MITL deck that the detector would sit on, the blast shield that the detector would against, and the spacer that can potentially separate the spectrometer from the liner.

To test the effects of each individual component, they were each modeled individually to determine their effects on $(S/B)_{dsr}$. The results of this are shown in Table 3.2.

As shown in Table 3.2, each individual component affects $(S/B)_{dsr}$ substantially. The coil-spacer routinely has line-of-sight (LOS) holes cut into them to accommodate diagnostics sensitive to the effects of neutron scattering and/or x-ray attenuation. Such a hole will be necessary for the neutron-recoil-spectrometer as well. The effects of this were modeled in MCNP6 by cutting cone-shaped holes of varying sizing through the coil-spacer. These cones were pointed at the detector and intersected at TCC. The results of this are shown in Figure 3-9.

As seen in Figure 3-9, a LOS hole in the coil-spacer of 1 cm max-diameter or more

Table 3.1: Parameters used in MCNP6 to model the geometry depicted in Figure 3-8. All cylinders are centered about TCC.

Coil Spacer	
Material	Titanium
Inner Diameter	4.62 cm
Outer Diameter	13.26 cm
Height	3.38"

Blast Shield	
Material	304 Stainless Steel
Inner Diameter	52.705 cm
Outer Diameter	55.88 cm
Height	20.32 cm
LOS Hole Height	10.16 cm
LOS Hole Width	5.08 cm

MITL Deck	
Material	Aluminum
Inner Diameter	76.53 cm
Outer Diameter	294.64 cm
Height	1.27 cm

Table 3.2: $(S/B)_{dsr}$ inferred from MCNP6 once external scattering sources are considered. Simulations were done without any external shielding and otherwise used parameters listed in Table 3.1 and Table 3.3.

Case	$(S/B)_{dsr}$
No External Sources	5.71
Spacer Modeled	1.95
Blast Shield Modeled	0.32
MITL Deck Modeled	0.24

increases $(S/B)_{dsr}$ by roughly 60%. This is much smaller than the size of LOS holes that are currently cut into the spacer for other diagnostics. A threshold-like behavior seems to occur when the solid angle of the hole matches that of the solid angle of

Figure 3-9: MCNP6 integrated down-scattered proton fluences in the case of a compressed liner (blue squares), in the case of no liner (yellow circles), and neutron-induced protons in the CR-39 (red diamonds) for varying sizes of LOS holes in the coil-spacer. The resultant $(S/B)_{dsr}$ from equation 3.3 is also shown as a black dashed curve. The compressed liners were compressed to 1.3 g/cm^2 and all other parameters were taken from Table 3.3. The spacer was the only external scattering source considered in these simulations.

the conversion-foil. This means that neutron-attenuation reducing the total signal is the dominant effect. It should be noted that the $(S/B)_{dsr}$ saturates at 3, which is still significantly lower than the value achieved with no external sources. This is due to neutron scattering from the entire spacer and can only be reduced linearly by reducing spacer material. It is noted again that in reality, several LOS holes are cut into the spacer, meaning this estimate is a lower bound on $(S/B)_{dsr}$.

The other way to mitigate the effects of external scatterings is using an external shield like the one shown in Figure 3-6. The neutron-spectrometer will use a polyethylene layer that surrounds the aluminum housing for this purpose. To determine the required thickness, MCNP6 simulations were done for many different thicknesses. For this study, all external scattering sources listed in Table 3.1 were included using appropriate LOS holes. The results of these simulations are shown in Figure 3-10.

Figure 3-10: MCNP6 integrated down-scattered proton fluences in the case of a compressed liner (blue squares), in the case of no liner (yellow circles), and neutron-induced protons in the CR-39 (red diamonds) for varying thicknesses of external shielding. The resultant $(S/B)_{dsr}$ from equation 3.3 is also shown as a black dashed curve. The compressed liners were compressed to 1.3 g/cm^2 and all other parameters were taken from Table 3.3. All sources of external scattering in Table 3.1 were considered in these simulations.

As shown in Figure 3-10, the neutron background drops roughly exponentially with the amount of shielding added as one would expect, while the added shielding has little impact on the measured signal. A $(S/B)_{dsr}$ greater than 1 can be achieved with at least 3 cm of external shielding.

3.3.3 Final Conceptual Design

After incorporating the shielding requirements, the final conceptual design of the neutron-recoil-spectrometer is described in Table 3.3. Additionally, the final predicted performance metrics are listed in Table 3.4 and example simulated spectra from this design are shown in Figure 3-11.

Figure 3-11: MCNP6 generated recoil-proton spectra on the detector of the next neutron-recoil-spectrometer designed for the Z facility. All parameters are taken from Table 3.1 using appropriate LOS holes and 3.3. The blue data show the spectra in the case of a Be liner compressed to 1.3 g/cm^2 and the yellow show the case where no liner is modeled.

3.3.4 Design Tolerances and Sensitivities

To understand the accuracy of the neutron-recoil-spectrometer, it's important to characterize how sensitive the various signals are to changes in the design parameters. The spectrometer is ultimately designed to measure both Y_{DDn} and dsr . Here we note:

$$Y_{\text{DDn}} \propto [P_1 + N]_{\text{meas}} - [N]_{\text{model}} \quad (3.4)$$

$$dsr \propto \frac{[P_2 + P_{\text{BG}} + N]_{\text{meas}} - [P_{\text{BG}} + N]_{\text{model}}}{[P_1 + N]_{\text{meas}} - [N]_{\text{model}}} \quad (3.5)$$

where our notation is defined by:

$$P_1 \equiv \int_{E_{dsr}}^{\infty} dE \phi_p^{\text{liner}} \quad (3.6)$$

$$P_2 \equiv \int_{E_{\min}}^{E_{dsr}} dE \phi_p^{\text{liner}} \quad (3.7)$$

$$P_{\text{BG}} \equiv \int_{E_{\min}}^{E_{dsr}} dE \phi_p^{\text{no-liner}} \quad (3.8)$$

$$N \equiv \int_0^{\infty} dE \eta_n \phi_n^{\text{liner}} \quad (3.9)$$

Note that equations 3.4 and 3.5 explicitly separate quantities that are actually

Table 3.3: Design parameters of the final conceptual design of the neutron-recoil-spectrometer. The slopes of the internal shield and the external surface of the housing is such that it would intersect with TCC if extended. The slopes of the internal surface of the housing and the external shielding match that of the external surface of the housing.

Internal Shield	
Material	Polyethylene
Max Diameter	5.0 cm
Length	50.0 cm
Conversion Foil	
Material	Polyethylene
Diameter	9.0 cm
Thickness	20.0 μm
Detector	
Material	CR-39
Diameter	5.0 cm
Thickness	1500 μm
Housing	
Material	Aluminum
Front Plate Distance from TCC	35.0 cm
Edge Distance from Foil	1.0 cm
Back Plate Distance from Detector	10.0 cm
Front Plate Thickness	0.5"
Mid Plate Thickness	100 μm
Back Plate Thickness	0.5"
External Thickness	0.5"
External Shield	
Material	Polyethylene
Thickness	6.0 cm

measured from the background components that have to be modeled. This is important because unknown changes in design parameters are not captured in the modeled

Table 3.4: Performance metrics for the next neutron-recoil-spectrometer. Simulations were done using parameters listed in Table 3.1 and Table 3.3.

Parameter	Value
Recoil-Protons	3200 per 10^{12} DD-n
Down-scattered Recoil-Protons (1.3 g/cm ² Liner)	2*280 per 10^{12} DD-n
Down-scattered Recoil-Protons (No Liner)	2*25 per 10^{12} DD-n
Neutron Induced Protons in CR-39	85 per 10^{12} DD-n
$(S/B)_{dsr}$	2.33

background subtractions. This treatment ensures that any changes in the background are properly reflected in any inferred sensitivities.

In this work, we define our sensitivities as the slope of the relative difference in Y_{DDn} or dsr caused by a change in a design parameter. Each parameter change is linearly fit over a specified range of values. Table 3.5 shows the results of this exercise to 8 design parameters.

Table 3.5: Design sensitivities for the next neutron-recoil-spectrometer. Sensitivities come from linear fits to several simulations within the specified range.

2*Parameter	Y_{DDn} (per cm)	dsr (per cm)	Range (cm)
Mid-Plate Thickness	-1.5%	-3.2%	[0.0, 1.0]
Front-Plate Distance to TCC	-4.3%	3.1%	[0.0, 5.0]
Spectrometer Alignment	-37.4%	28.3%	[0.0, 2.0]
Shield Length	-4.7%	-2.4%	[45.0, 55.0]
Shield Max Diameter	-30.2%	-34.6%	[5.0, 7.0]
Shield Alignment	-30.3%	81.6%	[0.1, 0.4]
Foil Diameter	34.4%	24.6%	[8.5, 9.5]
Detector Alignment	38.0%	246%	[0.0, 2.0]

Table 3.5 shows that the dsr measurement is particularly sensitive to the various alignments within the spectrometer. This is because if the detector clips the neutron "get lost cone", the neutron background can increase by orders of magnitude. However,

such a misalignment would likely be obvious in the data due to the spatial resolution of CR-39 and likely could be mitigated within the analysis.

3.4 Conclusions

In this work we have laid out the basic theory and requirements for a practical neutron recoil-spectrometer. This concept is of particular interest to the Z facility where the interpretation of traditional nToF measurements is challenged by a difficult neutron-scattering environment and long burn durations.

To this end, a proof-of-concept design was built and fielded on the Z facility. This was the first neutron-recoil-spectrometer ever fielded on Z, and the spectrometer was successfully used to measure a DDn spectrum. The yield inferred from these data was within a factor of 2 of the indium-activation measurements using simplified interpretations of the IRF. This measurement also demonstrated the necessity of neutron shielding in order to measure the dsr .

Finally, this work resulted in the design of a new shielded neutron-recoil-spectrometer capable of measuring dsr with $(S/B)_{dsr} > 2$. The new design is also capable of measuring the full spectrum with $(S/B) > 30$ over the primary DDn peak.

Data Availability Statement

The data that support the findings of this study are available from the corresponding author upon reasonable request.

Acknowledgments

The authors sincerely thank the Z facility operations staff who supported this work, and Bob Frankel and Ernie Doeg for processing the CR-39. This material is based upon work supported by the Department of Energy, National Nuclear Security Administration under Award Number DE-NA0003868, and by Sandia National Labo-

ratories contract number 2080471. Sandia National Laboratories is a multimission laboratory managed and operated by National Technology and Engineering Solutions of Sandia, LLC, a wholly owned subsidiary of Honeywell International Inc., for the U.S. Department of Energy's National Nuclear Security Administration under contract DE-NA0003525. This report was prepared as an account of work sponsored by an agency of the United States Government. Neither the United States Government nor any agency thereof, nor any of their employees, makes any warranty, express or implied, or assumes any legal liability or responsibility for the accuracy, completeness, or usefulness of any information, apparatus, product, or process disclosed, or represents that its use would not infringe privately owned rights. Reference herein to any specific commercial product, process, or service by trade name, trademark, manufacturer, or otherwise does not necessarily constitute or imply its endorsement, recommendation, or favoring by the United States Government or any agency thereof. The views and opinions of authors expressed herein do not necessarily state or reflect those of the United States Government or any agency thereof.

References

A | Secondary Reaction Energy Derivation

Consider the nuclear reaction:



We are interested in the final lab-frame energy of the product C in this reaction. This is given by:

$$E_C = \frac{1}{2}m_C|\vec{v}_c|^2 \quad (A.2)$$

where \vec{v}_C is the lab frame velocity and m_C is the mass of product C. The lab frame velocity is given by:

$$\vec{v}_C = \vec{u}_C + \vec{v}_{CM} \quad (A.3)$$

where \vec{u}_C is the center of mass velocity of product C and v_{CM} is the system's center of mass velocity given by:

$$\vec{v}_{CM} = \frac{m_A\vec{v}_A + m_B\vec{v}_B}{m_A + m_B} \quad (A.4)$$

The magnitude of \vec{u}_C is given by:

$$|\vec{u}_C| = \sqrt{\frac{2\mathcal{E}_C}{m_C}} \quad (A.5)$$

where \mathcal{E}_C is the center-of-mass energy of product C given by:

$$\mathcal{E}_C = \frac{m_D}{m_C + m_D} (Q + K) \quad (\text{A.6})$$

where Q is the energy gain of the reaction given by:

$$Q = (m_A + m_B - m_C - m_D) c^2 \quad (\text{A.7})$$

where c is the speed of light, and K is the kinetic energy given by:

$$K = \frac{1}{2} \mu (\vec{v}_A - \vec{v}_B)^2 \quad (\text{A.8})$$

and μ is the reduced mass given by:

$$\mu = \frac{m_A m_B}{m_A + m_B} \quad (\text{A.9})$$

If we assume $|\vec{v}_A| \ll |\vec{v}_B|$ (say in the case of a secondary nuclear reaction) then the only unknown is the direction of \vec{u}_C . We can rewrite equation A.2 in terms of θ , the angle between \vec{u}_C and \vec{v}_{CM} :

$$\begin{aligned} E_C &= \frac{1}{2} m_C |\vec{v}_c|^2 \\ &= \frac{1}{2} m_C (\vec{u}_C + \vec{v}_{CM})^2 \\ &= \frac{1}{2} m_C (|\vec{u}_C|^2 + |\vec{v}_{CM}|^2 + 2|\vec{u}_C||\vec{v}_{CM}|\cos\theta) \\ &= \frac{1}{2} m_C \left(\frac{2\mathcal{E}_C}{m_C} + \left(\frac{m_B}{m_A + m_B} \right)^2 |\vec{v}_B|^2 + 2\sqrt{\frac{2\mathcal{E}_C}{m_C}} \left(\frac{m_B}{m_A + m_B} \right) |\vec{v}_B| \cos\theta \right) \\ &= \frac{1}{2} m_C \left(\frac{2\mathcal{E}_C}{m_C} + \left(\frac{m_B}{m_A + m_B} \right)^2 \frac{2E_B}{m_B} + 2\sqrt{\frac{2\mathcal{E}_C}{m_C}} \left(\frac{m_B}{m_A + m_B} \right) \sqrt{\frac{2E_B}{m_B}} \cos\theta \right) \end{aligned} \quad (\text{A.10})$$

If we let $R_{AB} = \left(\frac{m_B}{m_A+m_B}\right)^2$ and $R_{CB} = \frac{m_C}{m_B}$, this reduces to:

$$E_C(\theta) = \mathcal{E}_C + R_{AB}R_{CB}E_B + 2\sqrt{R_{AB}R_{CB}E_B\mathcal{E}_C} \cos \theta \quad (\text{A.11})$$

This equation is maximized when $\theta = 0$. This is the case where the product C is born in the same direction as the center of mass momentum. Similarly, this equation is minimized when $\theta = \pi$ or when the product is born opposite the center of mass momentum. Using equation A.11 we can calculate the energy ranges of various secondary particles:

